

A SAFT equation of state for the quaternary $\text{H}_2\text{S}-\text{CO}_2-\text{H}_2\text{O}-\text{NaCl}$ system

Xiaoyan Ji^{a,*}, Chen Zhu^b

^a Energy Engineering, Division of Energy Science, Lulea University of Technology, 97187 Lulea, Sweden

^b Department of Geological Science, Indiana University, Bloomington, IN 47405, USA

Received 3 August 2011; accepted in revised form 18 May 2012; available online 26 May 2012

Abstract

Phase equilibria and thermodynamic properties of the quaternary $\text{H}_2\text{S}-\text{CO}_2-\text{H}_2\text{O}-\text{NaCl}$ system were studied using a statistical associating fluid theory (SAFT)-based equation of state (EOS) at temperatures from 0 to 200 °C (373.15–473.15 K), pressures up to 600 bar (60 MPa) and concentrations of NaCl up to 6 mol/kg H_2O . The understanding of the physical–chemical properties of this system is critical for predicting the consequences of co-injection of CO_2 and H_2S into geological formations (geological carbon sequestration) as an option for mitigating the global warming trend. Equation of state parameters were generated from regression of available and reliable experimental data and incorporation of existing parameters for some subsystems. Densities were predicted and compared with available experimental results. Using the EOS developed in this study, we predicted equilibrium compositions in both liquid and vapor phases, fugacity coefficients of components, the equilibrium pressures at a given composition of the H_2O -rich phase in electrolyte solutions with NaCl varying from 0 to 4 mol/kg H_2O , and the aqueous solution densities. These predicted values are tabulated and available as supplementary data in the electronic version online. These predictions provide information and guidance for future experiments regarding the thermodynamic properties and phase behaviors in the $\text{H}_2\text{S}-\text{CO}_2-\text{H}_2\text{O}-\text{NaCl}$ system.

© 2012 Elsevier Ltd. All rights reserved.

1. INTRODUCTION

Geologic carbon sequestration (GCS) is a promising option for the reduction of greenhouse gas emission into the atmosphere (IPCC, 2005). Co-injection of CO_2 and H_2S (e.g., from flue gases and natural gas fields) may substantially reduce the capture costs, but may also seriously increase the costs and risks of CO_2 transport and storage safety (Bachu and Bennion, 2009). Geochemically, the inclusion of even a small amount of H_2S can substantially change the formation water chemistry and, therefore, can alter the outcomes of water–rock interactions. As such, it is critical to study the behaviors and effects of H_2S impurities in the CO_2 stream in the GCS processes. Understanding

the phase equilibria and density of $\text{H}_2\text{S}-\text{CO}_2-\text{H}_2\text{O}$ -salts fluids (with Na, K, Ca, Mg, Cl, CO_3) at conditions pertinent to GCS (e.g., temperatures up to 200 °C and pressures up to 600 bars) is a critical step toward safety and cost benefit evaluations of transport and storage of mixed fluids.

H_2S is one of the most common components in natural gas and products from oil processing and production (Bachu et al., 2004). For example, the natural gas industry in the Alberta basin, Canada produces a significant amount of sour gases ($\text{H}_2\text{S} + \text{CO}_2$). Since surface desulphurization and surface storage is not economical and carries significant liability, acid gas (mixture of CO_2 and H_2S , also referred to as “sour gas”) disposal is operated through injection into depleted oil and gas reservoirs and deep saline formations (Bachu and Carroll, 2005). The first acid gas injection operation started in 1989, and according to the most recent count, 48 injection sites across the Alberta Basin and British Columbia are operating (Bachu and Gunter, 2004; IPCC, 2005; Bachu and Watson, 2009).

* Corresponding author. Tel.: +46 920 492837; fax: +46 920 491074.

E-mail address: xiaoyan.ji@ltu.se (X. Ji).

Nomenclature

\tilde{a}^{res}	dimensionless residual Helmholtz free energy	X	dimensionless quantity ($= \kappa d$)
$B_{\alpha\beta,i}$	bond fraction of type $\alpha\beta$ in molecule of component i	x_i (X_i)	mole fraction of component i
c_i	constant for calculating $k_{\alpha\beta}$, u/k , or cross association parameters ε and κ	x'_i	mole fraction of ion i on a solvent-free basis
c_{ij}	universal constants listed in Table A1	x_α	segment fraction
d	effective (hydrated) diameter	$X^{A_{zi}}$	mole fraction of molecule of component i not bonded at side A of segment α
D_{mn}	universal constants listed in Table A2	z_j	valence of the ion j
e	charge of an electron	Z	compressibility factor
$g_{\alpha\beta}^{\text{SW}}$	square-well radial distribution function	β	$1/kT$
k	Boltzmann constant	ε	well depth of the association site-site potential
$k_{\alpha\beta}$	binary interaction parameter	ε_w	dielectric constant of water
m	segment number	$\hat{\phi}_i$	fugacity coefficient of component i
m_i	number of segments of component i	κ^{AB}	parameter related to the volume available for bonding between sites A and B
N_{Av}	Avogadro number,	κ	Debye inverse screening length
$n(i)$	number of association sites on molecule i	λ	segment reduced range of the potential well
P	pressure in bar	$\lambda_{\alpha\beta}$	reduced range of the potential well for the α - β interaction
q_j	charge of ion j	ρ_m	molar density
T	absolute temperature in Kelvin	ρ_n	number density
T^*	dimensionless temperature ($= kT/u$)	ρ^*	reduced density
R	gas constant	σ_α	diameter of segment α
u	well depth of square-well potential	$z\sigma_{\alpha\beta}$	distance between centers of segment α and β at contact
u/k	segment energy	τ	close-packed reduced density ($= 2^{1/2} \pi/6$)
u_α	segment energy of segment α	$\Delta^{A_{zi}B_{\beta j}}$	association strength between site A_α at molecule of component i and site B_β at molecule of component j
$u_{\alpha\beta}$	well depth of square-well potential for the α - β interaction		
v^{oo}	segment volume		
v_α	molar volume of segment α		

However, a literature review of acid gas injection projects in western Canada revealed that most studies of the acid gas injection projects in Alberta Basin were qualitative (Buschkuehle and Michael, 2006; Bachu et al., 2008a,b; Micheal and Buschkuehle, 2008a,b); very limited quantitative analyses were conducted because quantitative analyses were hampered by the lack of equations of state that describes the physical chemical properties of mixed fluids for simulation. As a result, the few quantitative evaluations had to resort to *ad hoc* approaches in treating the properties of mixed fluids (Gunter et al., 2000; Knauss et al., 2005; Palandri and Kharaka, 2005; Xu et al., 2007; Xiao et al., 2009). For example, models had to include H₂S as dissolved in the liquid brine phase and co-injected with a separate CO₂ stream rather than as a mixed CO₂–H₂S gas stream. As field data and the experimental data of Bachu and Benion's (2009) show, chromatographic partitioning of H₂S in a dynamic system occurs because of the higher solubility of H₂S compared to that of CO₂. As a result, pure CO₂ breakthrough occurs first at the leading edges of a mixed CO₂–H₂S supercritical fluid plume, while H₂S is enriched in the brine that has been in contact with plume. Such physical phenomenon, observed both in field and laboratory experiments, currently cannot be modeled with the *ad hoc* approach. An equation of state is needed for reservoir

simulators to simulate phase behaviors and dynamic H₂S partitioning between different phases.

Experimental data are available for the ternary systems CO₂–H₂O–NaCl (see review in Ji et al. (2007)) and H₂S–H₂O–NaCl (see review in Duan et al. (2007)). However, to the best of our knowledge, no experimental data for the quaternary CO₂–H₂S–H₂O–NaCl system are publically available. Experiments to determine the equilibrium compositions and thermodynamic properties for systems containing H₂S are difficult, mainly because they are expensive and time consuming due to the corrosiveness of H₂S. Therefore, it is highly desirable to develop predictive models for exploring phase equilibria, densities, contaminant partitioning among liquid and gas phases, and other properties on the basis of available data from component subsystems, since these predictions can then provide valuable guides for future experiments.

Theoretically, two approaches have been used in modeling mixed fluid properties, namely the γ – ϕ approach and the ϕ – ϕ approach. Here γ denotes activity coefficient and ϕ stands for fugacity coefficient. In the γ – ϕ approach, an activity model is used to describe the non-ideality in the liquid phase and an equation of state (EOS) is used to describe the non-ideality in the vapor phase. The inherent disadvantage of this approach is that it does not allow for

estimates of the densities of the liquid phase. This approach has been used to develop models for the CO₂–H₂O–NaCl (Dubessy et al., 2005; Duan and Li, 2008; Spycher and Pruess, 2010), CO₂–H₂O (Spycher et al., 2003), and H₂S–H₂O and H₂S–H₂O–salt (Dubessy et al., 2005; Duan et al., 2007) systems.

In the ϕ – ϕ approach, an EOS is used for both phases. This approach has been applied to CO₂–H₂O, H₂S–H₂O, and H₂S–CO₂ systems. For example, Perfetti and co-workers (Perfetti et al., 2008a,b) and Li and Firoozabadi (2009) used cubic plus association EOS for the CO₂–H₂O and H₂S–H₂O systems; Pappa et al. (2009) used the Peng–Robinson EOS for the CO₂–H₂O system; Sun and Dubessy (2010) used statistical associating fluid theory (SAFT)–LJ for CO₂–H₂O; dos Ramos and McCabe (2010) used the SAFT–VR–D for H₂S–H₂O; and Tang and Gross (2010) used PCP–SAFT for the H₂S–CO₂ system.

However, to the best of our knowledge, no EOS has been developed for the quaternary H₂S–CO₂–H₂O–NaCl system with any approaches. Our previous work on the binary and ternary subsystems used the ϕ – ϕ approach. A SAFT EOS was used to describe the phase equilibria and density for H₂S–H₂O (Ji and Zhu, 2010) and CO₂–H₂O–NaCl (Ji et al., 2005a) and the properties of the aqueous electrolyte solutions with the ions of Na⁺, K⁺, Ca²⁺, Mg²⁺, Cl[–], and CO₃^{2–} (Ji et al., 2005b, 2006; Ji and Adidharma, 2006, 2007, 2008; Tan et al., 2006). Building on the previous work, here we used a SAFT EOS to represent the phase behaviors for the H₂S–CO₂–H₂O–NaCl system. The resulting EOS can then be coupled with process simulation models, e.g., multi-phase flow and reactive transport models to provide a more reliable prediction. Although co-injection of CO₂ and H₂S has been simulated in the literature, models were developed in the absence of an EOS for the H₂S–CO₂–H₂O–NaCl system, and an *ad hoc* approach had to be used (e.g., injecting H₂S in the aqueous phase, not injecting CO₂–H₂S gas mixtures, (Xu et al., 2007)). The development of an EOS in this study is the first step toward reliable long-term prediction pertaining to geological carbon sequestration, such as sequestration capacity, CO₂ leakage, environmental impacts, etc.

2. SAFT EQUATION OF STATE AND PARAMETER EVALUATIONS

SAFT EOS is a promising EOS to describe the phase equilibria and properties for the systems of interest in this study. In our previous work, SAFT1–RPM (Ji et al., 2005a) was used to describe the phase equilibria and properties for CO₂–H₂O and CO₂–H₂O–NaCl systems. After that, SAFT1–RPM was improved to SAFT2 (Tan et al., 2006) to describe the phase equilibria and properties for aqueous electrolyte solutions (Tan et al., 2006; Ji and Adidharma, 2007), aqueous mixed-electrolyte solutions (Ji et al., 2005b, 2006; Ji and Adidharma, 2006, 2008), CO₂–ionic liquids (Ji and Adidharma, 2009, 2010, 2012), and H₂S–H₂O (Ji and Zhu, 2010) systems. In this work, SAFT2 was extended to the quaternary H₂S–CO₂–H₂O–NaCl system.

In both SAFT1 and SAFT2, square-well (SW) fluid is used as a reference. The SW fluid has a steep repulsion

and a short-range attraction. Three parameters, the hard core diameter (σ), the well depth (u) and the reduced range of the potential well (λ), were used to characterize the SW potential model, and the intermolecular potential ϕ is defined as:

$$\phi(r) = \begin{cases} \infty & r < \sigma \\ -u & \sigma \leq r \leq \lambda\sigma \\ 0 & r > \sigma \end{cases}$$

The molecule in SAFT1 or SAFT2 is modeled as a chain of m tangentially bonded spherical segments, and association sites are assigned to account for hydrogen bonding, and long-range electrostatic interaction is taken into account for charged molecules. The SAFT EOS accounts for molecular interactions in terms of Helmholtz free energy. For SAFT2, the dimensionless residual Helmholtz energy is defined as:

$$\tilde{a}^{\text{res}} = \tilde{a}^{\text{hs}} + \tilde{a}^{\text{disp}} + \tilde{a}^{\text{chain}} + \tilde{a}^{\text{assoc}} + \tilde{a}^{\text{ion}} \quad (1)$$

where the superscripts refer to terms accounting for the residual, hard-sphere, dispersion, chain, association, and ionic interactions, respectively. Each term has been described in our previous work and summarized in the [Appendix A](#).

Any other thermodynamic properties can be calculated from this residual Helmholtz energy. For example, the fugacity coefficient of component i can be derived as:

$$\ln \hat{\phi}_i = \tilde{a}^{\text{res}} + \left(\frac{\partial \tilde{a}^{\text{res}}}{\partial x_i} \right)_{T, \rho, x_{j \neq i}} - \sum_j x_j \left(\frac{\partial \tilde{a}^{\text{res}}}{\partial x_j} \right)_{T, \rho, x_{k \neq j}} + Z - 1 - \ln Z \quad (2)$$

where Z is compressibility factor and calculated with

$$Z = 1 + \rho \left(\frac{\partial \tilde{a}^{\text{res}}}{\partial \rho} \right)_{T, x} \quad (3)$$

3. RESULTS AND DISCUSSIONS

Equations with $X_i = 1$ and $x_\alpha = 1$ are applied to pure components. For neutral components, there are four parameters: segment number m , segment volume v^{oo} , segment energy u/k , and the reduced range of the potential well λ . For ionic (charged) components, there is one more parameter, effective diameter d . For the components with association interactions, two additional parameters are needed: the well depth of the association site–site potential ε and the parameter related to the volume available for bonding κ .

In our previous work, the properties for H₂S (Ji and Zhu, 2010), CO₂ (Ji and Adidharma, 2010), H₂O (Tan et al., 2006), NaCl–H₂O (Ji and Adidharma, 2007), and H₂S–H₂O (Ji and Zhu, 2010) were investigated with SAFT2. For completeness, the model results are summarized in the [Appendix B](#). The properties and phase equilibrium for CO₂–H₂O and CO₂–H₂O–NaCl were investigated with SAFT1–RPM (Ji et al., 2005a). Since SAFT2 is an improvement of SAFT1–RPM, the parameters of SAFT2 were obtained from the fitting of the same experimental data with exactly the same method as in the previous work

Table 1
Cs in Eqs. (4)–(6), (and) (9).

Parameter	Value	Parameter	Value	Parameter	Value
C_1	6.5349×10^2	C_3	3.72163×10^{-2}	C_5	-4.2800×10^{-1}
C_2	1.783×10^{-3}	$C_4 \text{ (K}^{-1}\text{)}$	5.5909×10^{-7}	$C_6 \text{ (K}^{-1}\text{)}$	1.6560×10^{-3}

(Ji et al., 2005a). The new fitted results are also summarized in the Appendix B.

3.1. $\text{H}_2\text{S}(1)\text{--CO}_2(2)$

For $\text{H}_2\text{S}(1)\text{--CO}_2(2)$, we assumed that there was only one type of cross association, i.e. between the site of type H in H_2S and the site of type O in CO_2 . Since the self-association in pure H_2S and CO_2 is of different origin, i.e. only the former is due to hydrogen bonding, we prefer not to use the common mixing rules for the association parameters. The cross association parameters were directly fitted to the experimental data and found to be constant

$$\frac{\epsilon_{12}^{\text{HO}}}{k} = C_1 \quad (4)$$

$$\kappa_{12}^{\text{HO}} = C_2 \quad (5)$$

where Cs are constants, k is the Boltzmann constant, $\epsilon_{12}^{\text{HO}}$ is the well depth of the site-site interaction potential energy between a site of type H in component 1 and a site of type O in component 2, and κ_{12}^{HO} is a measure of the volume available for bonding between a site of type H in component 1 and a site of type O in component 2.

A temperature-dependent binary interaction parameter k_{12} is used to adjust the cross dispersive energy for this binary system.

$$k_{12} = C_3 + C_4 T \quad (6)$$

For the $\text{H}_2\text{S}\text{--CO}_2$ system, the phase equilibrium has been measured by Bierlein and Kay (1953) at 20, 30, 40, 50,

60, 70, and 80 atm and temperatures up to 363.15 K. Sobocinski and Kurata (1959) also measured the phase equilibrium under similar conditions. Stouffer et al. (2001) determined the densities experimentally at temperatures between 220 and 450 K and at pressures up to 25 MPa both in the single-phase region and in the liquid + vapor two-phase region. The vapor–liquid phase boundary conditions were determined by locating the deviations from smooth (p , T) behavior.

To obtain the parameters of $C_1\text{--}C_4$, the phase equilibrium experimental data were used. The fitted results are listed in Table 1 with an average relative deviation of 1.7%. The comparison of model results with the experimental data is shown in Figs. 1 and 2. The model results agree well with the experimental data in both phases.

With the obtained parameters, the densities in the single phase region were predicted from the temperature, pressure, and a certain isomole of CO_2 ($x_{\text{CO}_2} = 0.9393, 0.9045, 0.7067$, and 0.5001 , respectively). Since the temperature of interest in this work is higher than 273.15 K, densities were predicted at temperatures higher than 273.15 K and compared with the available experimental results from Stouffer et al. (2001), as shown in Figs. 3–6, respectively.

At $x_{\text{CO}_2} = 0.9393$, the model prediction agrees well with experimental data at temperatures up to 350 K and pressures up to 20 MPa (200 bar) except at one data point at 309.943 K and 7.8057 MPa. Here, the model prediction is 6091 mol/m³ while the experimental result is 7253 mol/m³.

At $x_{\text{CO}_2} = 0.9045$, the model prediction agrees well with experimental data throughout the whole temperature and

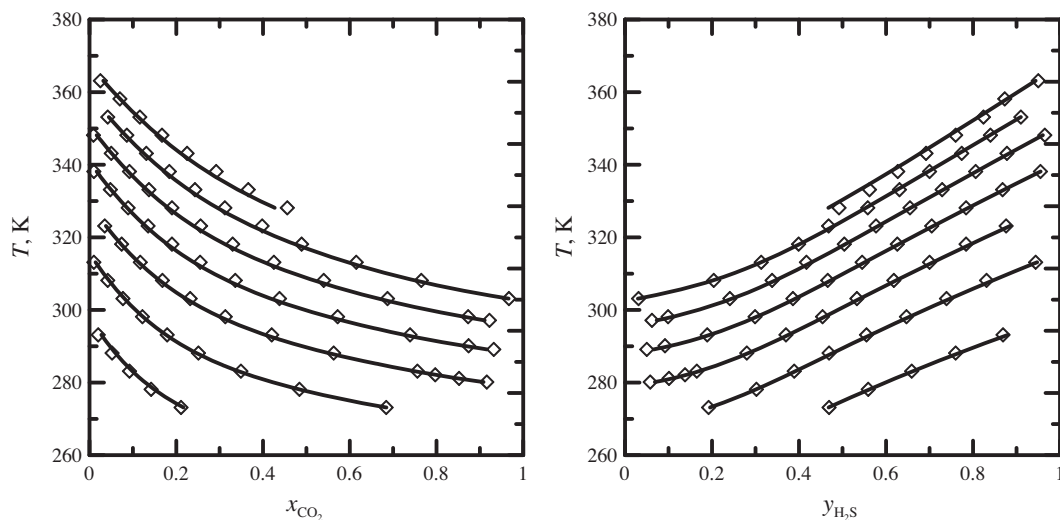


Fig. 1. Comparison of the results at equilibrium calculated with the model with the experimental data of Bierlein and Kay (1953) at 80.04, 70.91, 60.78, 50.65, 40.52, 30.39, and 20.26 bar from up to down. ◇: experimental data; curves: calculations in this study.

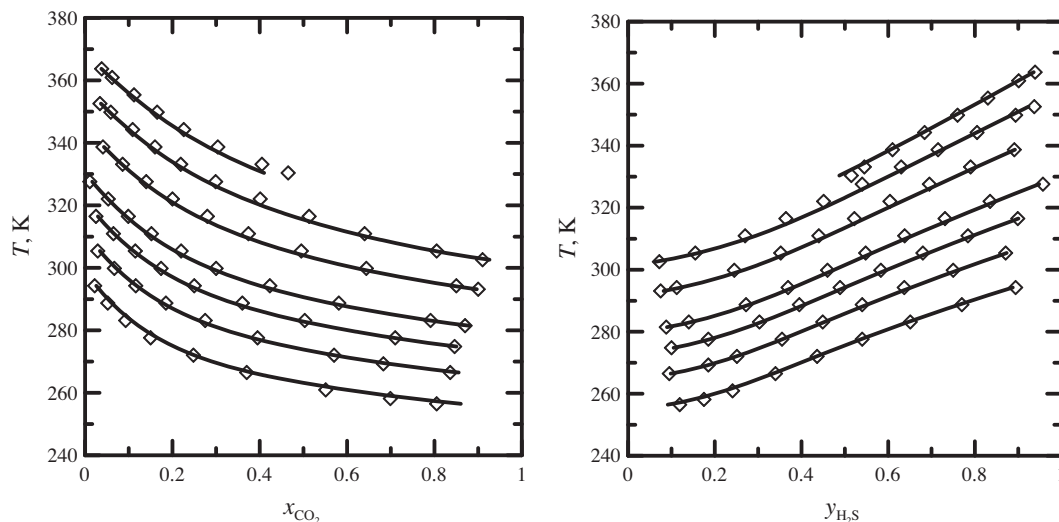


Fig. 2. Comparison of the results at equilibrium calculated with the model with the experimental data of Sobocinski and Kurata (1959) at 82.74, 68.95, 55.16, 41.37, 34.47, 27.58, and 20.68 bar from up to down. \diamond : experimental data; curves: calculations in this study.

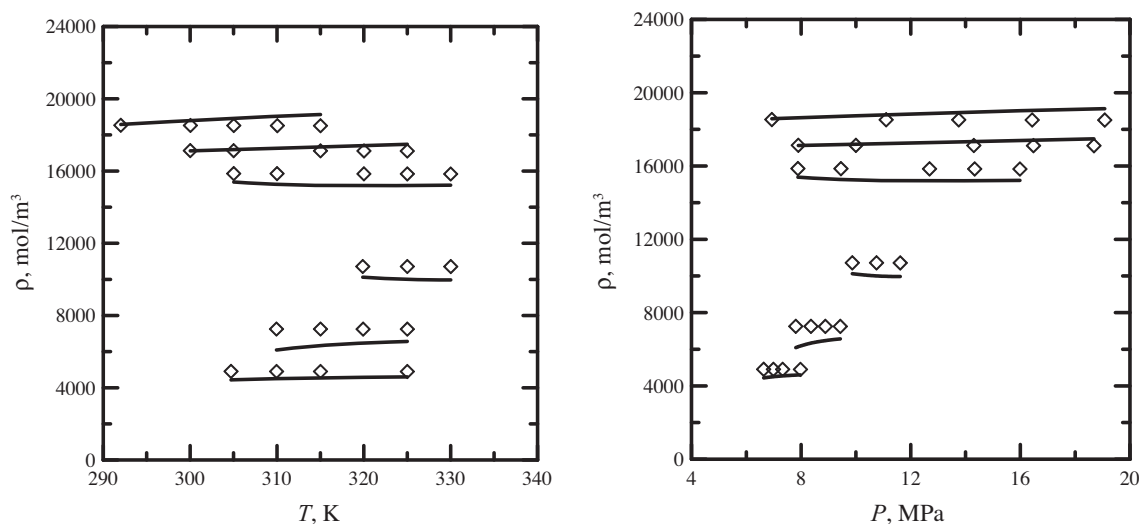


Fig. 3. Comparison of predicted densities in the single phase region with the experimental data of Stouffer et al. (2001) ($x_{\text{CO}_2} = 0.9393$). \diamond : experimental data; curves: independent predictions in this study.

pressure range. Similarly excellent comparison results are obtained for both $x_{\text{CO}_2} = 0.7067$ and $x_{\text{CO}_2} = 0.5001$.

With the model and obtained parameters, the saturation compositions and densities at equilibrium in both phases were predicted under fixed temperature and pressure. The model prediction of the composition in both phases agrees extremely well with the experimental data from Stouffer et al. (2001), as shown in Figs. 7–10. For the density in both phases, there are some discrepancies around the vicinity of the critical temperature and pressure of CO_2 . As we discussed previously (Ji and Zhu, 2010), for pure component, as with other versions of SAFT, the underlying mean-field theory causes the model in this study to slightly overestimate the critical point. This may be one reason for the discrepancies in density.

When the mole fraction of H_2S is much less than that of CO_2 , the model shows similar observations in the vicinity of critical temperature and pressure of CO_2 , i.e. the model overestimates the critical point, as shown in Fig. 7. When the mole fraction of H_2S increases, the model representation of the critical point becomes more accurate, as shown in Fig. 8. In Figs. 9 and 10, the model represents the critical point quite well.

Figs. 7–10 are different from other figures in that the symbols represent predicted compositions and the dashed lines are experimental values. In the experiments, the saturated pressures were estimated at fixed mole fraction of CO_2 (a linear curve in figures) and temperature. In modeling, the compositions were calculated from T and P .

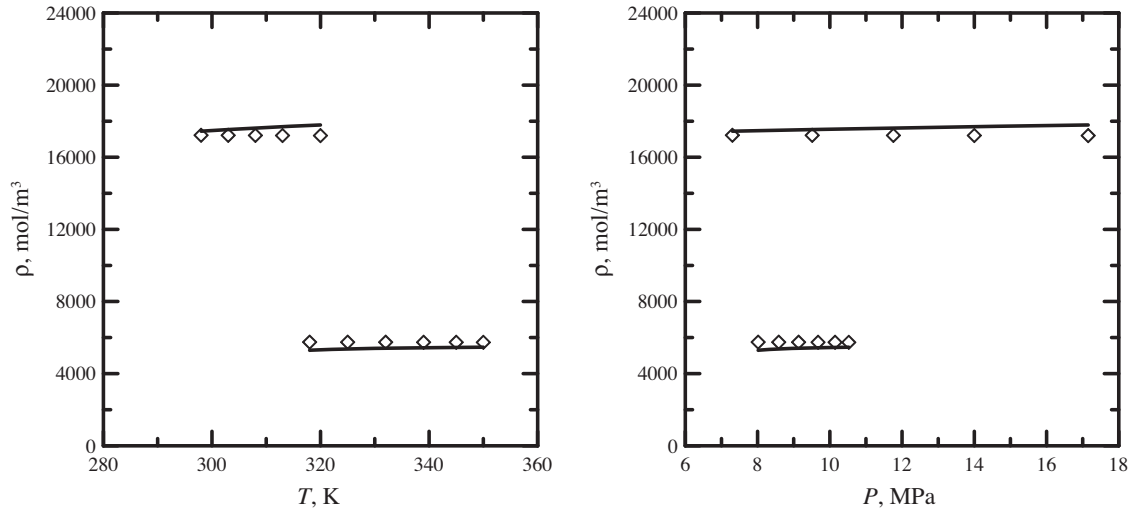


Fig. 4. The comparison of the predicted densities in the single phase region with the experimental data of [Stouffer et al. \(2001\)](#) ($x_{\text{CO}_2} = 0.9045$). \diamond : experimental data; curves: independent predictions in this study.

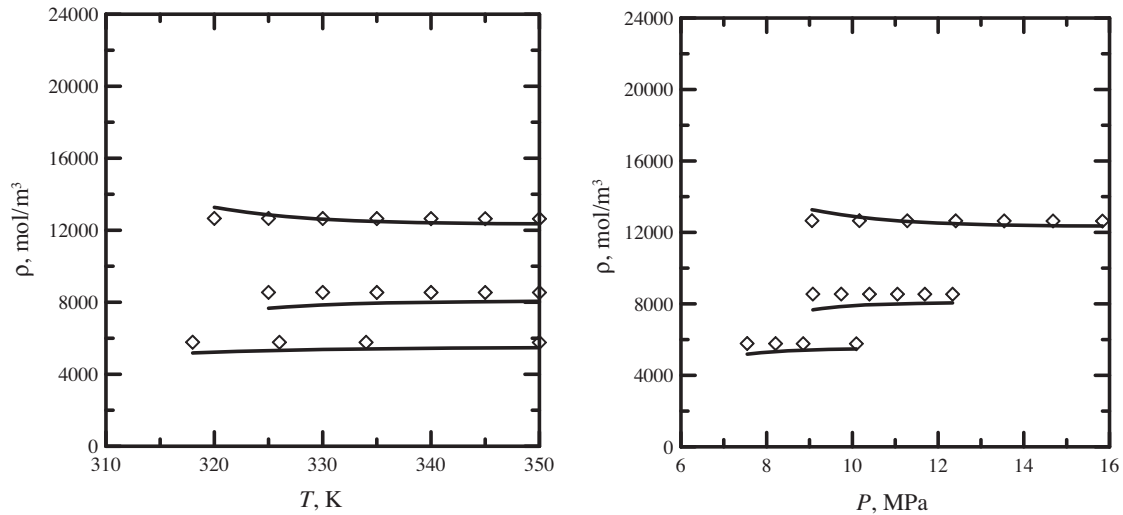


Fig. 5. The comparison of the predicted densities in the single phase region with the experimental data of [Stouffer et al. \(2001\)](#) ($x_{\text{CO}_2} = 0.7067$). \diamond : experimental data; curves: independent predictions in this study.

3.2. $\text{H}_2\text{S}(1)\text{--}\text{H}_2\text{O}(3)\text{--}\text{NaCl}(4)$

Modeling of this ternary system was built on the work by [Ji and Zhu \(2010\)](#) on $\text{H}_2\text{S}\text{--}\text{H}_2\text{O}$ and on the work by [Ji and Adidharma \(2007\)](#) on $\text{H}_2\text{O}\text{--}\text{NaCl}$. In this study, one additional binary interaction constant, the same k_{14} , was used for both $\text{H}_2\text{S}\text{--}\text{Na}^+$ and $\text{H}_2\text{S}\text{--}\text{Cl}^-$ pairs to adjust the short-range interactions between segments H_2S and Na^+/Cl^- ,

$$u_{14+} = (u_{14+})^{1/2}(1 - k_{14}) \quad (7)$$

$$u_{14-} = (u_{14-})^{1/2}(1 - k_{14}) \quad (8)$$

where subscripts 4+ and 4– denote the Na^+ and Cl^- , respectively.

The temperature-dependent cross parameter was allowed with the following equation:

$$k_{14} = c_5 + c_6/T \quad (9)$$

For $\text{H}_2\text{S}(1)\text{--}\text{H}_2\text{O}(3)\text{--}\text{NaCl}(4)$, the available experimental data have been summarized in the work by [Duan et al. \(2007\)](#), and the experimental data by [Xia et al. \(2000\)](#) have been proved to be reliable. [Xia et al. \(2000\)](#)'s experimental data cover a wide range of temperature, pressure, and molality of NaCl . Thus, the experimental data from [Xia et al. \(2000\)](#) were used to obtain the coefficients in Eq. (9). The fitted results are listed in Table 1.

The comparison of the model results with the experimental data by [Xia et al. \(2000\)](#) is shown in Fig. 11. The

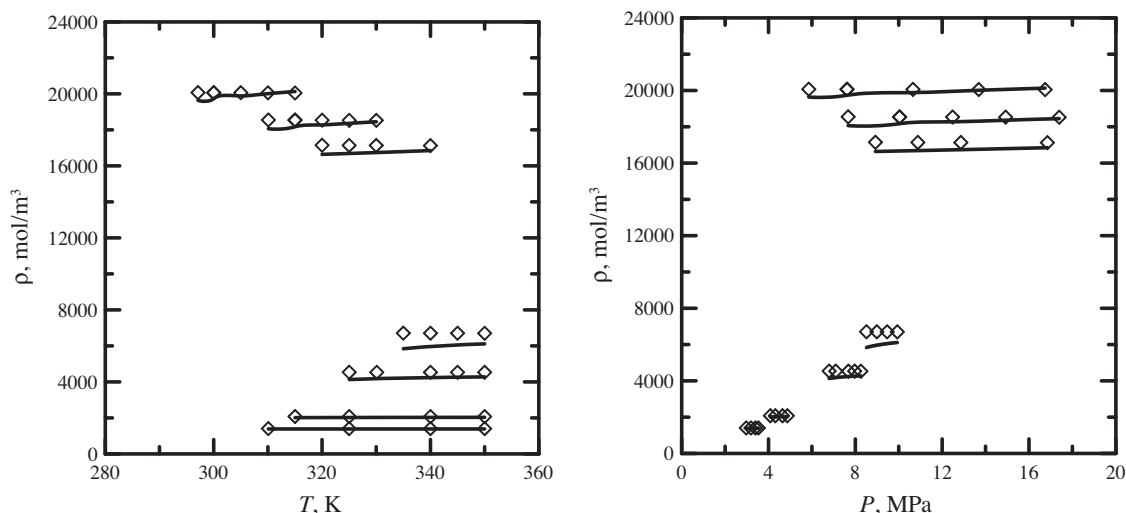


Fig. 6. The comparison of the predicted densities in the single phase region with the experimental data of Stouffer et al. (2001) ($x_{\text{CO}_2} = 0.5001$). \diamond : experimental data; curves: independent predictions in this study.

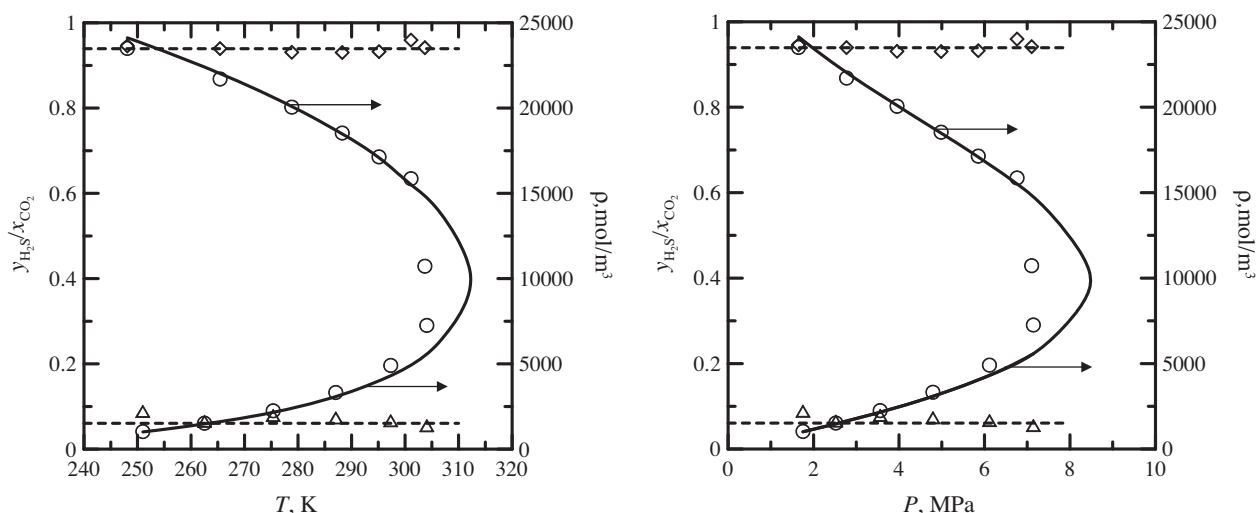


Fig. 7. Comparison of predicted composition and density at equilibrium with the experimental data of Stouffer et al. (2001). \circ , densities from Stouffer et al.; solid curves: density prediction in this study. Dash curves: $x_{\text{CO}_2} = 0.9393$ and $y_{\text{H}_2\text{S}} = 0.0607$ from Stouffer et al. (2001); \diamond , predicted composition of CO_2 in the liquid phases (x_{CO_2}); \triangle , predicted composition of H_2S in the vapor phases ($y_{\text{H}_2\text{S}}$).

H_2S solubility in NaCl solutions increases with increasing pressure, decreasing temperature and decreasing concentration of NaCl . This phenomenon is well captured with our model.

Below we will compare predictions from our model for the $\text{H}_2\text{S}(1)\text{--H}_2\text{O}(3)\text{--NaCl}(4)$ system with experimental data that were not used in the parameter fitting. H_2S solubility in aqueous NaCl solutions and H_2O mole fraction in the vapor phase were determined by Suleimenov and Krupp (1994) at temperatures from 428 to 594 K and pressures up to 140 bar. The comparison of the model results with the experimental data is listed in Table 2. Although the temperatures in this group of experimental data are much higher than those we used to obtain the model parameters, our model nevertheless gives a very good prediction for the H_2S

solubility in aqueous NaCl solutions. Furthermore, the experimental data that we used for parameter fitting in the model have only the compositions of the liquid phases. However, model prediction of compositions in the vapor phase compare well to the experimental data, which suggests that our model is a reliable way to predict compositions for $\text{H}_2\text{S}(1)\text{--H}_2\text{O}(3)\text{--NaCl}(4)$ in both phases.

Barrett et al. (1988) measured H_2S solubility in aqueous NaCl solutions at one bar, concentrations of NaCl (m_{NaCl}) of 0, 1, 2, 3, 4, and 5 mol/kg H_2O , and temperatures from 25 to 95 °C. The model predictions were compared with this group of experimental data. The comparison at 0, 2, and 5 mol/kg H_2O of NaCl is shown in Fig. 12.

Drummond (1981) measured the H_2S solubility in aqueous NaCl solutions ($m_{\text{NaCl}} = 1, 2, 4$, and 6 mol/kg H_2O) and

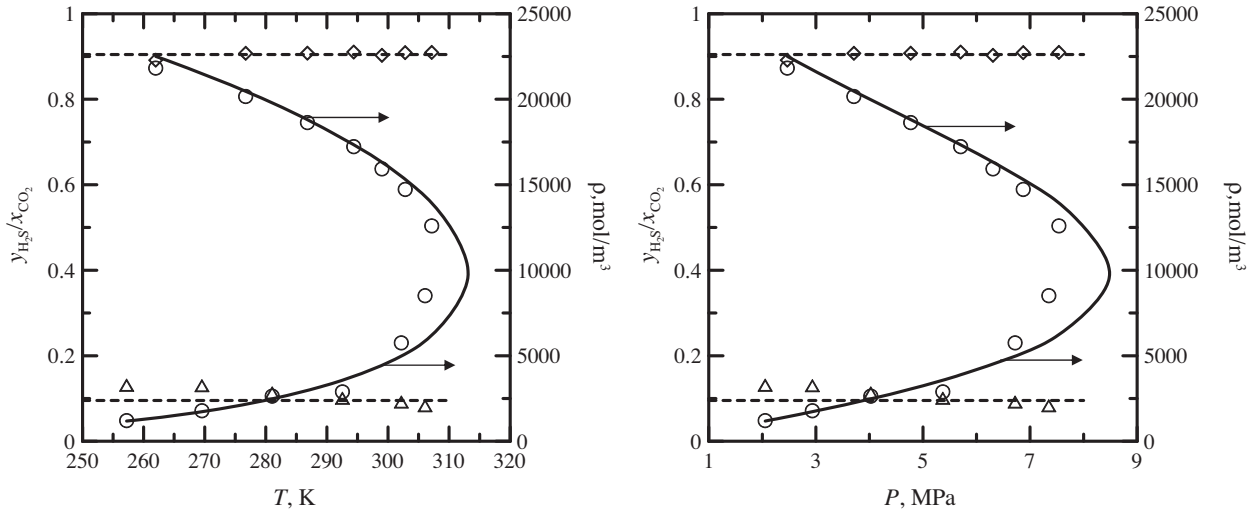


Fig. 8. Comparison of predicted composition and density at equilibrium with the experimental data of [Stouffer et al. \(2001\)](#) (see also in [Ji and Zhu \(2010\)](#)). \circ , densities from [Stouffer et al.](#); solid curves: density prediction in this studies; for compositions, dash curves: $x_{\text{CO}_2} = 0.9045$ and $y_{\text{H}_2\text{S}} = 0.0955$ from [Stouffer et al. \(2001\)](#); \diamond , predicted composition of CO_2 in the liquid phases (x_{CO_2}); \triangle , predicted composition of H_2S in the vapor phases ($y_{\text{H}_2\text{S}}$).

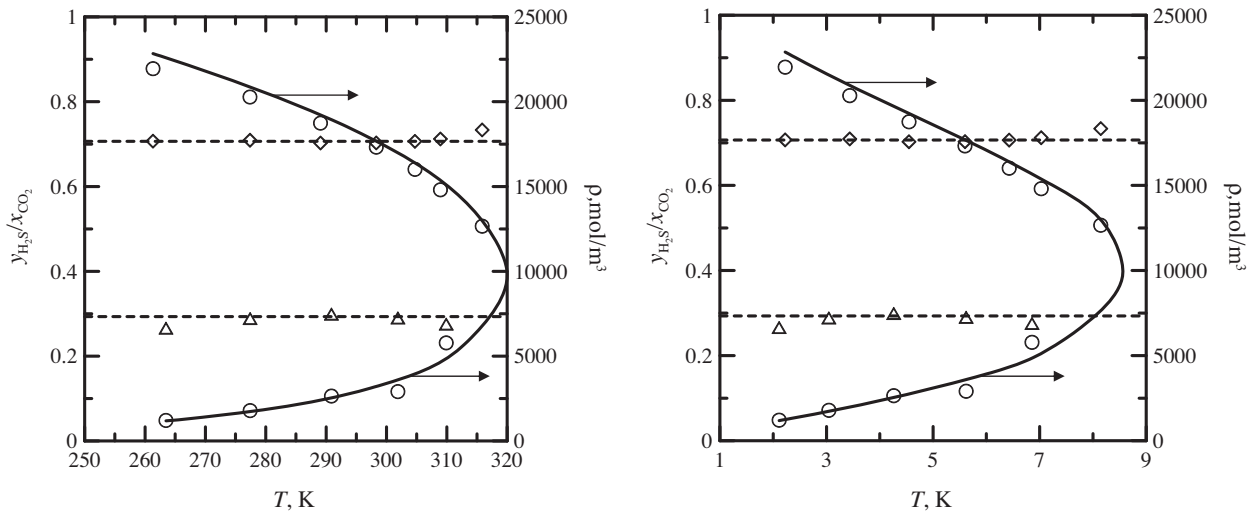


Fig. 9. Comparison of predicted composition and density at equilibrium with the experimental data of [Stouffer et al. \(2001\)](#) (see also in [Ji and Zhu \(2010\)](#)). \circ , densities from [Stouffer et al. \(2001\)](#); solid curves: density prediction in this work; for compositions, dash curves: $x_{\text{CO}_2} = 0.7067$ and $y_{\text{H}_2\text{S}} = 0.2933$ from [Stouffer et al. \(2001\)](#); \diamond , predicted composition of CO_2 in the liquid phases (x_{CO_2}); \triangle , predicted composition of H_2S in the vapor phases ($y_{\text{H}_2\text{S}}$).

the corresponding H_2O mole fractions in the vapor phases. At $m_{\text{NaCl}} = 1$ and $2 \text{ mol/kgH}_2\text{O}$, the experimental data were measured in the cooling and heating processes, while the other experimental data ($m_{\text{NaCl}} = 4$ and $6 \text{ mol/kgH}_2\text{O}$) were measured in the heating process only. The comparison of the model results at $m_{\text{NaCl}} = 1$, and $2 \text{ mol/kgH}_2\text{O}$ with the experimental data of [Drummond \(1981\)](#) measured in both processes is shown in [Fig. 13a](#), in which the filled symbols represent the experimental data from the cooling process, while the hollow symbols represent the experimental data from the heating process and the vertical axis represents the relative error $[(x_{\text{exp}} - x_{\text{cal}})/x_{\text{exp}}]$ between the

experimental data (x_{exp}) and the calculation results (x_{cal}). The data measured in different processes show large discrepancies, and the experimental data measured in heating processes are more consistent with results calculated with model.

The comparison of the experimental data measured in the heating process with the model predictions at other concentrations of NaCl ($m_{\text{NaCl}} = 4$ and $6 \text{ mol/kgH}_2\text{O}$) is shown in [Fig. 13b](#), where the vertical axis again represents the relative error between the experimental data and calculation results. To show the overall results with the data measured in the heating process, the corresponding comparisons at

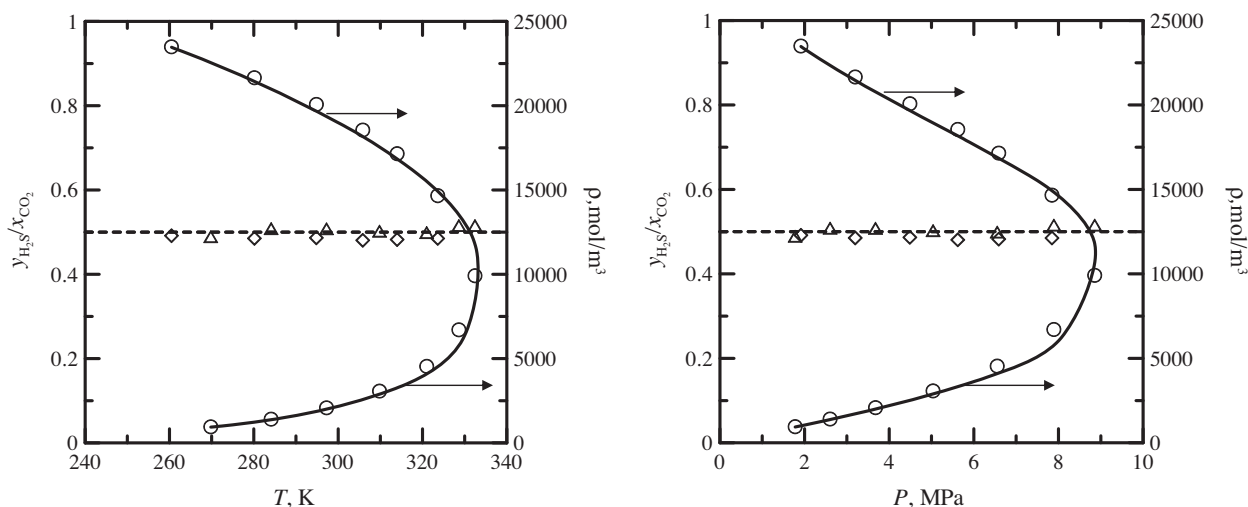


Fig. 10. Comparison of predicted composition and density at equilibrium with the experimental data of Stouffer et al. (2001) (see also in Ji and Zhu (2010)). \circ , densities from Stouffer et al. (2001); solid curves: density prediction in this study; for compositions, dash curves: $x_{\text{CO}_2} = 0.5001$ and $y_{\text{H}_2\text{S}} = 0.4999$ from Stouffer et al.; \diamond , composition of CO_2 in the liquid phases (x_{CO_2}) predicted with the model; \triangle , composition of H_2S in the vapor phases ($y_{\text{H}_2\text{S}}$) predicted with the model.

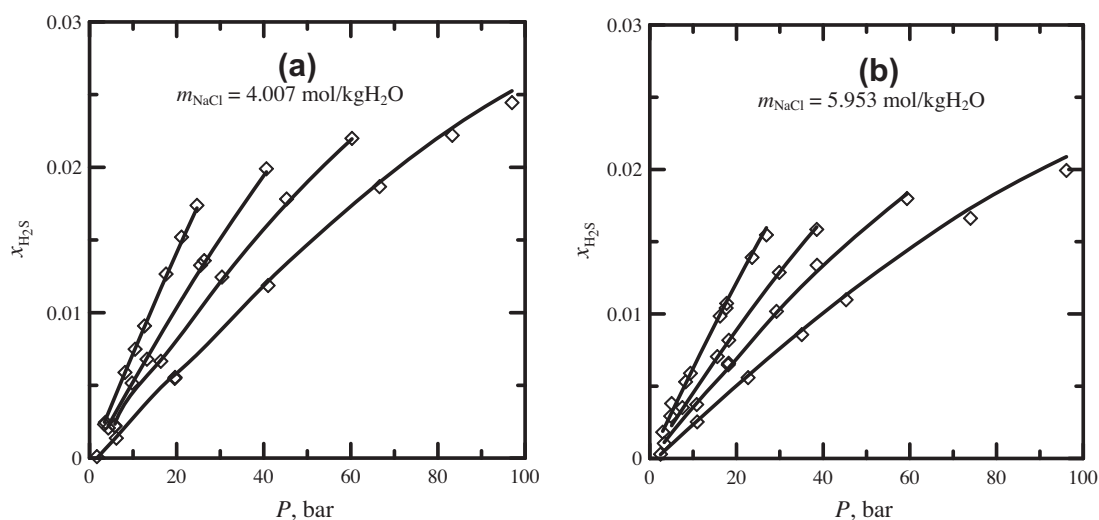


Fig. 11. Comparison of calculated H_2S solubility in aqueous NaCl solutions with the data of Xia et al. (2000) at 313.15, 333.15, 353.15, and 393.15 K from left to right with different concentrations of NaCl . \diamond , experimental data from Xia et al. (2000); curves: calculations in this study.

$m_{\text{NaCl}} = 1$ and $2 \text{ mol/kgH}_2\text{O}$ are also illustrated in Fig. 13b. The discrepancies between experimental data measured in the heating process and modeling results in this study are less than 20%, which are similar to those in Duan et al. (1996).

Our model also predicted well the H_2O composition in the vapor phases (the mixture of $\text{H}_2\text{S} + \text{H}_2\text{O}$) when compared with the experimental data (Fig. 14). Note that the model predictions at high temperatures and pressures are not as good as those at lower temperatures and pressures. The model parameter was fitted to experimental data at much lower temperatures, but nevertheless the predictions up to 673 K and pressure up to 300 bar held up reasonably well.

3.3. $\text{H}_2\text{S}(1)\text{--CO}_2(2)\text{--H}_2\text{O}(3)\text{--NaCl}(4)$

Thus far, we have collected parameters for the four components (H_2S , CO_2 , H_2O , and NaCl) which are necessary for predicting phase equilibrium and properties for the quaternary $\text{H}_2\text{S}\text{--CO}_2\text{--H}_2\text{O}\text{--NaCl}$ system. We obtained the parameters of H_2S , CO_2 , and H_2O from their density and saturation pressure, and we obtained parameters of NaCl from the $\text{NaCl}\text{--H}_2\text{O}$ system. Cross parameters between each two component pairs were fitted from the respective subsystem systems: $\text{H}_2\text{S}\text{--CO}_2$, $\text{H}_2\text{S}\text{--H}_2\text{O}$, $\text{H}_2\text{S}\text{--H}_2\text{O}\text{--NaCl}$, $\text{CO}_2\text{--H}_2\text{O}$, $\text{CO}_2\text{--H}_2\text{O}\text{--NaCl}$; specifically, cross parameters of $\text{H}_2\text{S}\text{--CO}_2$ from $\text{H}_2\text{S}\text{--CO}_2$ system; $\text{H}_2\text{S}\text{--H}_2\text{O}$ from $\text{H}_2\text{S}\text{--H}_2\text{O}$ system; $\text{H}_2\text{S}\text{--NaCl}$ from $\text{H}_2\text{S}\text{--H}_2\text{O}\text{--NaCl}$ system;

Table 2

Comparison of the model prediction with the experimental data from Suleimenov and Krupp (1994).

T (K)	P (Bar)	m_{NaCl} (mol/kgH ₂ O)	$x_{\text{H}_2\text{S}}$			$y_{\text{H}_2\text{O}}$		
			Exp.	Cal.	$x_{\text{exp}} - x_{\text{cal}}$	Exp.	Cal.	$y_{\text{exp}} - y_{\text{cal}}$
428.45	11.96	0.5036	0.0027	0.0028	−0.0001	0.4623	0.4656	−0.0033
428.35	12.14	0.9209	0.0027	0.0028	−0.0001	0.4481	0.4516	−0.0035
428.45	12.37	1.2704	0.0026	0.0028	−0.0002	0.4359	0.4394	−0.0035
428.55	12.65	1.5691	0.0026	0.0028	−0.0002	0.4233	0.4267	−0.0035
428.55	12.92	1.8176	0.0026	0.0028	−0.0002	0.4112	0.4145	−0.0033
428.55	13.12	2.0355	0.0027	0.0028	−0.0002	0.4020	0.4052	−0.0033
428.45	13.42	2.2271	0.0027	0.0029	−0.0002	0.3897	0.3928	−0.0031
428.45	13.71	2.3937	0.0028	0.0029	−0.0002	0.3796	0.3825	−0.0029
428.35	14.05	2.5421	0.0028	0.0030	−0.0002	0.3680	0.3706	−0.0026
489.65	27.6	0.2394	0.0024	0.0026	−0.0002	0.7916	0.7977	−0.0062
489.65	27.58	0.6429	0.0023	0.0025	−0.0002	0.7811	0.7884	−0.0073
489.55	27.46	0.9752	0.0023	0.0024	−0.0002	0.7734	0.7819	−0.0084
489.45	27.43	1.2567	0.0023	0.0024	−0.0001	0.7649	0.7743	−0.0094
489.45	27.48	1.4979	0.0023	0.0024	−0.0001	0.7568	0.7671	−0.0103
489.55	27.56	1.7046	0.0023	0.0024	−0.0001	0.7502	0.7612	−0.0110
489.45	27.7	1.8889	0.0024	0.0024	−0.0001	0.7403	0.7518	−0.0115
489.45	27.87	2.0523	0.0024	0.0025	−0.0001	0.7316	0.7435	−0.0119
593.95	137.86	0.5340	0.0147	0.0131	0.0016	0.8875	0.8401	0.0474
593.65	137.38	0.9524	0.0132	0.0123	0.0009	0.8732	0.8313	0.0419
593.75	137.21	1.2933	0.0124	0.0116	0.0009	0.8626	0.8263	0.0363
593.65	137.54	1.5822	0.0118	0.0112	0.0006	0.8505	0.8186	0.0319
593.55	137.9	1.8243	0.0115	0.0110	0.0005	0.8397	0.8118	0.0279
593.55	138.42	2.0305	0.0114	0.0108	0.0006	0.8302	0.8058	0.0245

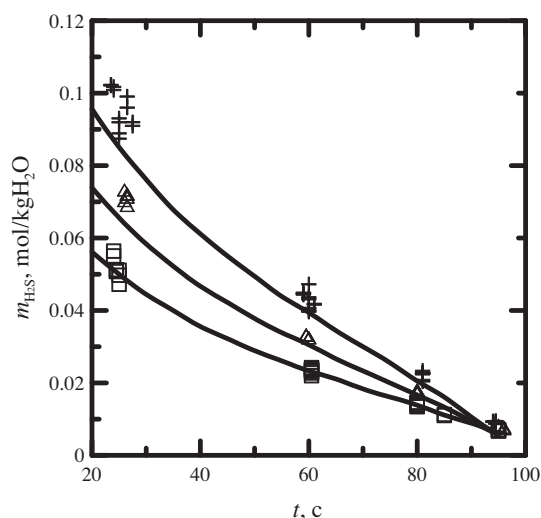


Fig. 12. Comparison of model predicted H₂S solubility in aqueous NaCl solutions with the experimental data of Barrett et al. (1988) at one bar. +, experimental data at $m_{\text{NaCl}} = 0$; Δ , at $m_{\text{NaCl}} = 2$ mol/kgH₂O; \square , at $m_{\text{NaCl}} = 5$ mol/kgH₂O; curves: calculation from the model developed in this study. Note: these experimental data were not used in the parameter fitting of the model.

CO₂–H₂O from CO₂–H₂O system; and CO₂–NaCl from CO₂–H₂O–NaCl system.

Once we had these parameters, we could predict properties for the quaternary system. SAFT generally considers the interaction between two molecules, and there is no need to include the interaction for three bodies. However, predic-

tion accuracy depends on the reliability of the parameters we obtained. As such, to get better representation, sometimes the cross parameters needed to fit to the quaternary system directly.

3.4. Predictions from the New EOS

As we mentioned in Section 1, one motivation for the development of a SAFT-based EOS for the quaternary system is the lack of experimental data. As a result, no direct comparison between EOS predictions and experimental data is possible. Bachu and Bennion (2009) conducted solubility measurements in the H₂S–CO₂–brine system, but their experimental data collection was incomplete for parameter fitting for the quaternary system and only part of their data can be compared with equilibrium composition predictions. Bachu and Bennion (2009) ran experiments representing the field conditions at an injection site into the Keg River Formation in Northern Alberta at 334.15 K, 135 bar and with a salinity of 118,950 mg/L. During the experiment, they prepared the brine and then titrated a H₂S–CO₂ gas mixture into the apparatus containing the brine while agitating it. They observed the bubbling points, but did not record them. They continued to titrate more gas mixture into the chamber in order to simulate the process of injection. After a certain time period, they removed the “excess gas” and measured the CO₂ and H₂S as a percentage of dissolved gases in the liquid phase.

Assuming that the brine is a solution with NaCl only, our model was used to predict the gas solubility at the specific mole percentage listed in the work of Bachu and

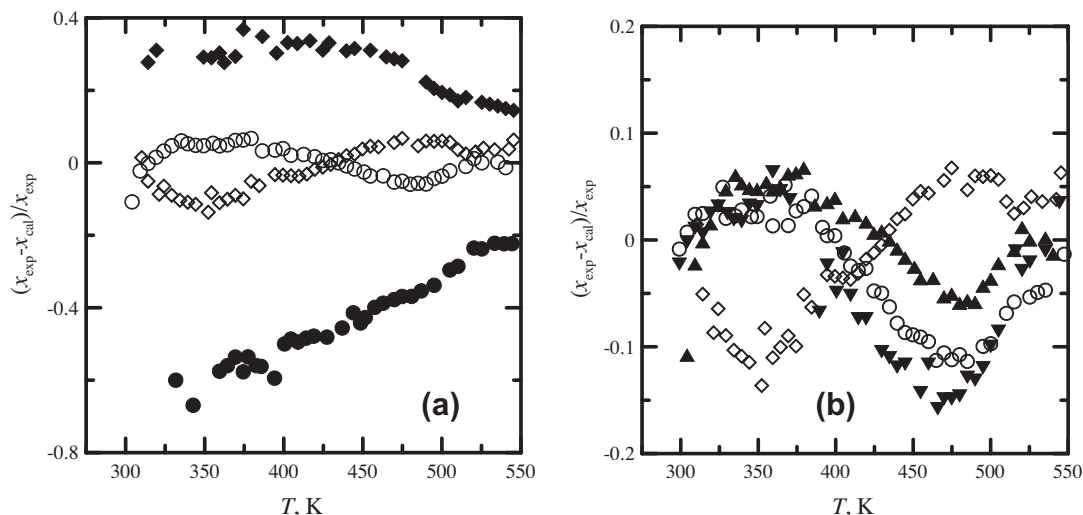


Fig. 13. Comparison of the H_2S solubility in aqueous NaCl solutions with the data of Drummond (1981). \diamond , $m_{\text{NaCl}} = 1 \text{ mol/kgH}_2\text{O}$ in the heating process; \blacklozenge , $m_{\text{NaCl}} = 1 \text{ mol/kgH}_2\text{O}$ in the cooling process; \circ , $m_{\text{NaCl}} = 2 \text{ mol/kgH}_2\text{O}$ in the heating process; \bullet , $m_{\text{NaCl}} = 2 \text{ mol/kgH}_2\text{O}$ in the cooling process; \blacktriangle , $m_{\text{NaCl}} = 4 \text{ mol/kgH}_2\text{O}$ in the heating process; \blacktriangledown , $m_{\text{NaCl}} = 6 \text{ mol/kgH}_2\text{O}$ in the heating process; vertical axis represents the relative error $[(x_{\text{exp}} - x_{\text{cal}})/x_{\text{exp}}]$ between the experimental data (x_{exp}) and calculation results (x_{cal}).

Bennion (2009). The prediction results are shown in Table 3. For pure CO_2 –brine (NaCl – H_2O), the measurements of CO_2 solubility from Bachu and Bennion (2009) is 0.0134 (mole fraction), the prediction from this study is 0.0139, and the result from the model of Duan and Li (2008) is 0.0135. All these results are in good agreement. For pure H_2S –brine (NaCl – H_2O), the measurement of H_2S solubility (Bachu and Bennion, 2009) is 0.0344 (mole fraction), the prediction from this work is 0.0276, and the result from the model of Duan et al. (2007) is 0.0301. There are some discrepancies, but no other experimental data can be used to verify the results.

From the composition of liquid, temperature and pressure, the composition of the contact gas at equilibrium can be predicted. The results are listed in the second column from right in Table 3. The mole fraction of CO_2 in the vapor phase is higher than that in the liquid, which implies that H_2S is more soluble than CO_2 . This prediction agrees with the experimental observation of Bachu and Bennion (2009).

When the gas mixture is titrated until reaching the bubble pressure, the mole fraction in the solution should be the same as the gas mixture injected. There is no vapor phase. Injecting additional contact gas (called excess gas in Bachu and Bennion (2009)) broke the established equilibrium and a new equilibrium was reached after certain time. Also, the CO_2 , H_2S , and H_2O were redistributed at the new equilibrium. If the amount of “excess gas” is sufficiently large, the equilibrium gas composition was the same as the injection gas (consistent with the limiting case of an infinite reservoir). This is the case in most experiments (Table 3). If the amount of “excess gas” is small (finite external reservoir), the gas compositions in the vapor phase change according to equilibrium partitioning, with the more water soluble gas (H_2S) enriched in the liquid phase and the less water soluble gas (CO_2) enriched in

the vapor phase. The amounts of “excess gas” were not reported in Bachu and Bennion (2009), but for the experiments with 70% and 50% CO_2 in injection mixture, the predicted equilibrium fractions in the vapor phase, 76% and 52%, respectively are higher than that in the injection mixture. The enrichment of CO_2 at equilibrium with respect to the initial injection gas is consistent with the discussion above on the preferentially higher solubility of H_2S than of CO_2 . In addition, densities of the liquid at equilibrium were predicted and listed in the last column of Table 3.

Generally, for acid gas injection, the injection depths of the operations range from 824 to 3432 m, *in situ* temperatures vary from 29 °C to 110 °C, and pressure changes vary from 6.6 to 35.9 MPa (Bachu and Carroll, 2005). The composition of the injected acid gas varies from 2% to 83% H_2S and 95% to 14% CO_2 , with no more than trace percentages of hydrocarbon gases, such as methane, ethane, propane, etc. (Bachu and Carroll, 2005). In this study, our model can be used to predict the saturation composition in both phases and the corresponding densities, as well as the density in the single phase region (unsaturated fluid mixtures). The gas solubility is important for predicting the sequestration capacity, and for predication calculations, we assume that all the gas mixture has been dissolved into solutions and the mole ratio of H_2S to CO_2 in the solution is the same as that of the injection gas. We also can assume that the mole ratio of H_2S to CO_2 in the gas-rich phase to be constant, such as in the situation of an infinite gas reservoir near the well bore.

With the obtained parameters, the properties and phase equilibria for the H_2S – CO_2 – H_2O – NaCl system were predicted. Equilibrium pressures were predicted from the mole fraction in the H_2O -rich phase at the temperature of interest. In calculations, the mole ratio of H_2S to CO_2 was fixed as 0.5 in the H_2O -rich phase, the concentration of NaCl varied

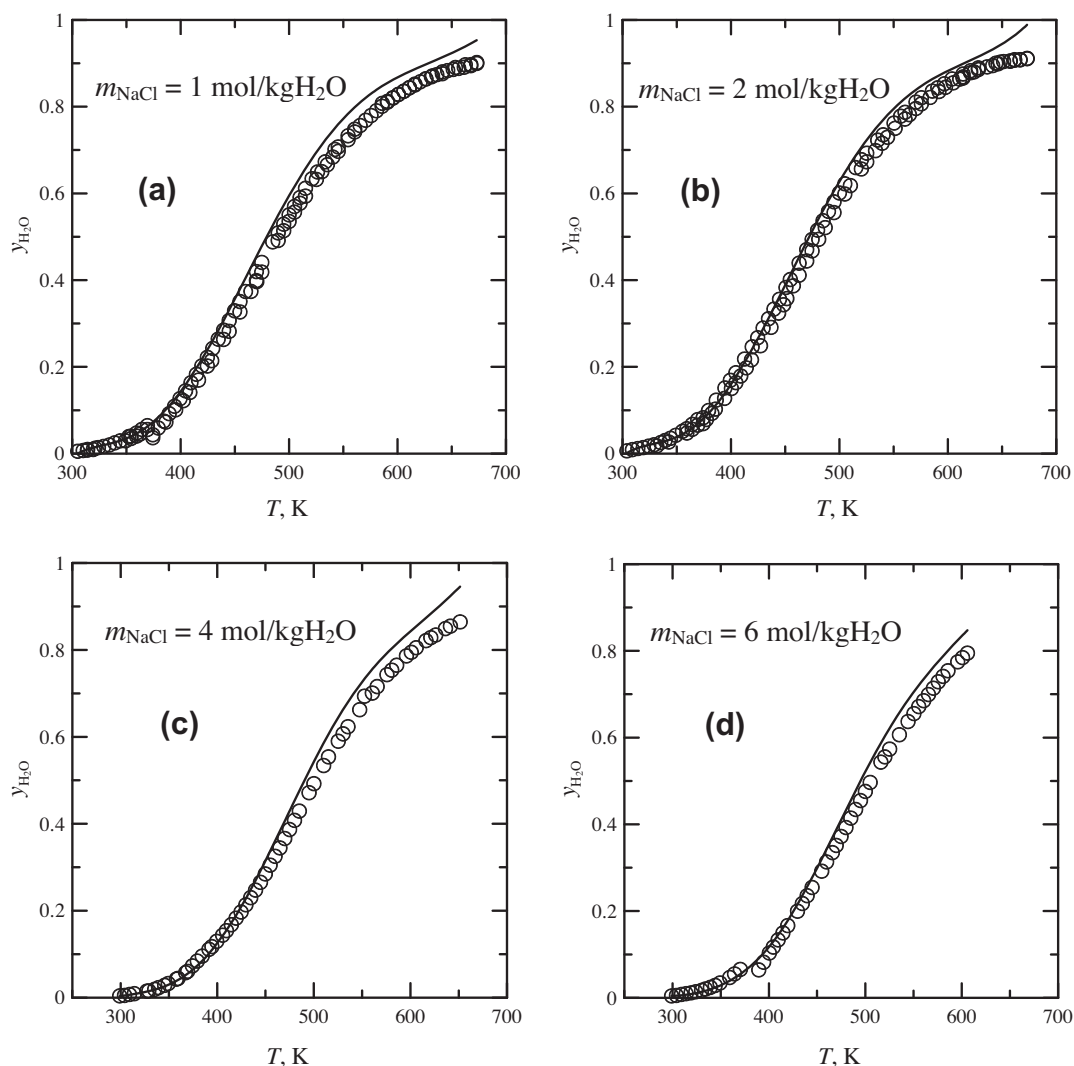


Fig. 14. The comparison of the H_2O concentration in the vapor phase with the data of Drummond (1981). \diamond : experimental data; curves: model prediction in this study.

Table 3

Gas solubility, density, and contact gas composition at 334.15 K, 135 bar, salinity of 118950 mg/L ($m_{\text{NaCl}} = 2.05 \text{ mol/kgH}_2\text{O}$).

Liquid composition Dry basis		Solubility of gas mixture Mole fraction			Contact gas X_{CO_2} Dry basis		Density (kg/m^3)
CO_2	H_2S	Exptl	Pred'ed	Duan et al.	Inj gas	At eq.	Pred'ed
100	0	0.0134	0.0139	0.0135	100	100	1066.5
74.41	25.59	0.0151	0.0172		90	89.11	1065.5
56.58	43.42	0.0193	0.0203		70	76.53	1064.5
36.39	63.61	0.0240	0.0247		50	52.00	1062.7
22.85	77.15	0.0272	0.0269		30	29.33	1061.1
9.09	90.91	0.0315	0.0277		10	9.44	1059.3
0	100	0.0344	0.0276	0.0301	0	0	1058.3

from 0, 1, 2 to 4 mol/kg H_2O , and the temperature was set as 298.15, 323.15 and 348.15 K.

Equilibrium pressures for the H_2S – CO_2 – H_2O system at 298.15 K were compared with those for H_2S – H_2O and

CO_2 – H_2O (Fig. 15a). At a given mole fraction in the H_2O -rich phase, the equilibrium pressure of CO_2 is much higher than that for H_2S , which means that H_2S is more soluble than CO_2 . For the mixture of $(\text{H}_2\text{S} + \text{CO}_2)$ – H_2O , at

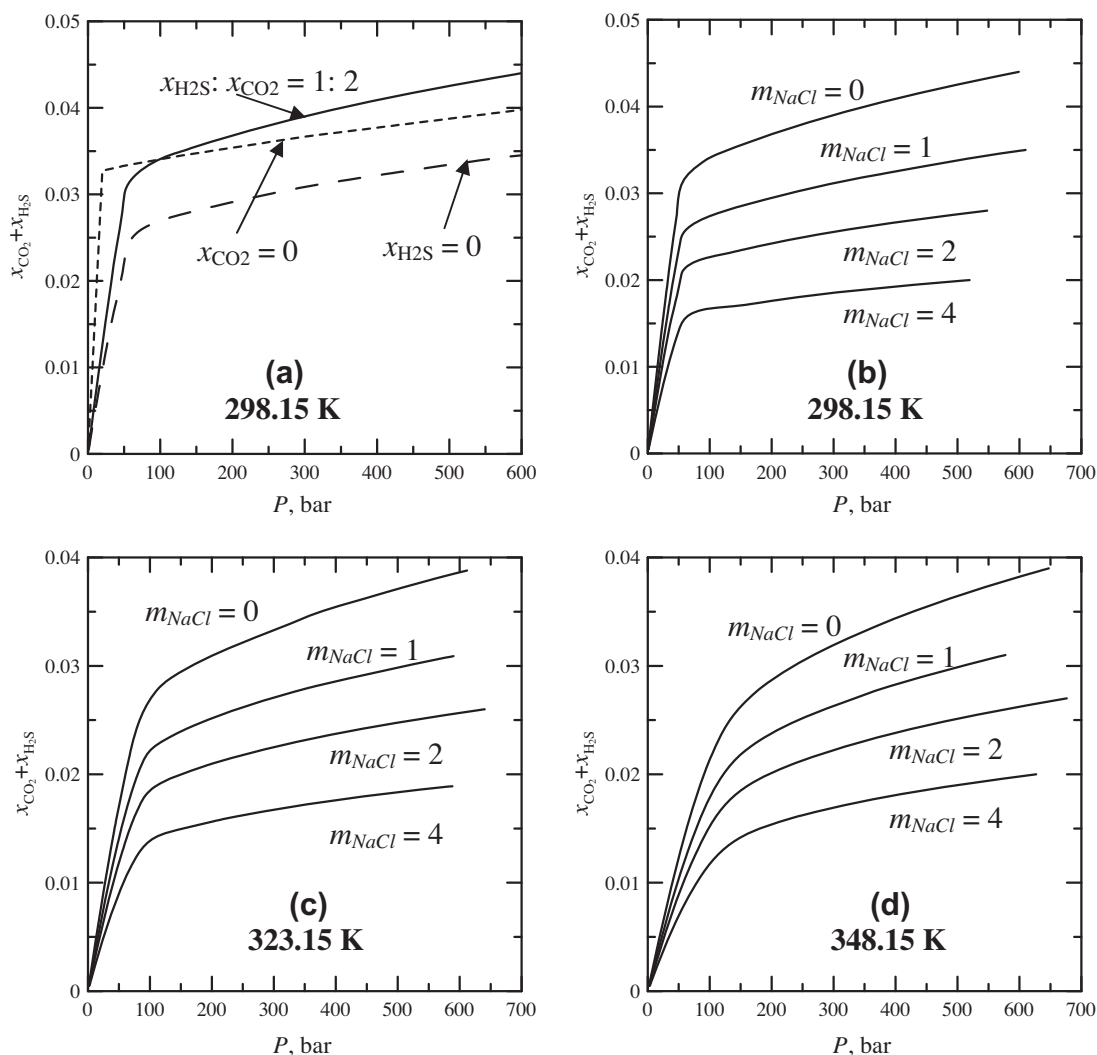


Fig. 15. The equilibrium pressure versus concentration of $(\text{H}_2\text{S} + \text{CO}_2)$ in the H_2O -rich phase.

low concentrations of $(\text{H}_2\text{S} + \text{CO}_2)$, equilibrium pressure for the mixture is between those for $\text{H}_2\text{S}-\text{H}_2\text{O}$ and $\text{CO}_2-\text{H}_2\text{O}$. While at high $(\text{H}_2\text{S} + \text{CO}_2)$ concentrations, equilibrium pressure for the $(\text{H}_2\text{S} + \text{CO}_2 + \text{H}_2\text{O})$ mixture is the lowest for all mixtures, which means the $(\text{H}_2\text{S} + \text{CO}_2)$ mixture is more soluble than pure H_2S and CO_2 . The predicted equilibrium pressures for $\text{H}_2\text{S}-\text{H}_2\text{O}$ and $\text{CO}_2-\text{H}_2\text{O}$ have been verified with available experimental data. However, there are no experimental data available for $\text{H}_2\text{S}-\text{CO}_2-\text{H}_2\text{O}$. Moreover, the results show that the solubility of the gas mixture is not a linear combination of the two pure gases, indicating interference with the solubility of each other, which underscores the need for an EOS.

Equilibrium pressures for the $\text{H}_2\text{S}-\text{CO}_2-\text{H}_2\text{O}-\text{NaCl}$ system at 298.15, 323.15 and 348.15 K with different molality of NaCl (m) were predicted and shown in Fig. 15b–d. The equilibrium pressure increases with increasing concentrations of the $(\text{H}_2\text{S} + \text{CO}_2)$ mixture and increasing concentrations of NaCl. At 298.15 K, it is obvious that with increasing pressure, the concentration of $(\text{H}_2\text{S} + \text{CO}_2)$ in-

creases significantly and then levels off, which imply a change of phase equilibrium from vapor-liquid equilibrium to liquid-liquid equilibrium. However, with increasing temperature, this phenomenon becomes weak. For example, the pressure continuously affects the concentration of $(\text{H}_2\text{S} + \text{CO}_2)$ at 348.15 K and low concentration of NaCl. Spycher and Pruess (2010) show that in the $\text{CO}_2-\text{H}_2\text{O}-\text{NaCl}$ system, the immiscibility between $\text{CO}_2-\text{H}_2\text{O}$ rich phases decrease with increasing temperature. Fig. 15 suggests a similar temperature dependence of the immiscibility of a H_2O -rich phase and gas-rich phase in the system $\text{H}_2\text{S}-\text{CO}_2-\text{H}_2\text{O}-\text{NaCl}$.

It is well known that density differential can cause vertical convection in the reservoir (Yang and Gu, 2006). Previous research shows that, with CO_2 dissolution, the aqueous solution density becomes denser, which can induce natural convection and hence enhance CO_2 dissolution (solubility trapping) in the reservoir (Yang and Gu, 2006). The co-injection of H_2S complicates the matter. However, until now, it was not possible to predict the solution density as

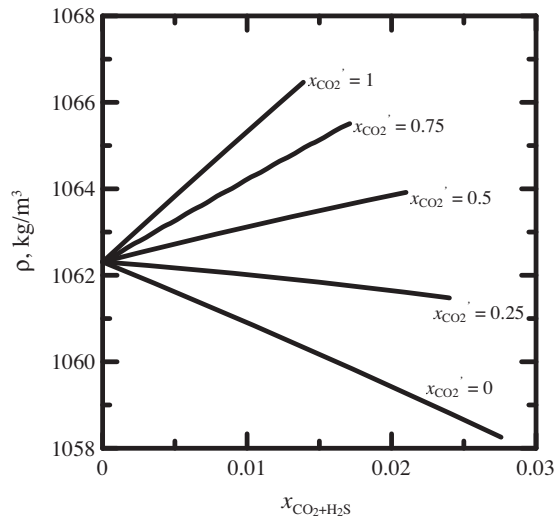


Fig. 16. Density of the solution H_2S – CO_2 – H_2O – NaCl at 334.15 K, 135 bar and $m_{\text{NaCl}} = 2.05 \text{ mol/kgH}_2\text{O}$.

a result from dissolution of both CO_2 and H_2S . Using the model of this study, the density of H_2S – H_2O – NaCl and H_2S – CO_2 – H_2O – NaCl fluids is predicted at different temperature, pressure and composition. The calculations show that the density of the solution becomes lighter due to the dissolution of H_2S , which is the opposite of the effect of CO_2 on the solution density. Fig. 16 shows the solution density at 334.15 K, 130 bar, $m_{\text{NaCl}} = 2.05 \text{ mol/kgH}_2\text{O}$, and the mole fraction of gases from zero to saturated concentration for H_2S – CO_2 – H_2O – NaCl solutions in which $x_{\text{CO}_2} = x_{\text{CO}_2}/(x_{\text{CO}_2} + x_{\text{H}_2\text{S}}) = 0, 0.25, 0.5, 0.75$ and 1. At $x_{\text{CO}_2} = 0$, i.e. solutions of H_2S – H_2O – NaCl , the solution density decreases when the concentration of H_2S increases. While at $x_{\text{CO}_2} = 1$, i.e. solutions of CO_2 – H_2O – NaCl , the solution density increases when the concentration of CO_2 increases. For the gas mixture, when the mole fraction of H_2S increases, the solution density decreases.

4. CONCLUSIONS

Here we report the development of a statistical associating fluid theory (SAFT)-based equation of state (EOS) for the quaternary H_2S – CO_2 – H_2O – NaCl system. To the best of our knowledge, there is no EOS for this quaternary system, and it is therefore the first of its kind. To obtain cross parameters of SAFT, the phase equilibria and thermodynamic properties for H_2S – CO_2 and H_2S – H_2O – NaCl systems were investigated, while parameters for other subsystems were obtained from previous work (see the Appendix B).

Using the EOS in this study, we are now able to predict phase equilibria and properties in the H_2S – CO_2 – H_2O – NaCl system. Our predictions show that the dissolved concentration of $(\text{H}_2\text{S} + \text{CO}_2)$ mixture increases with increasing pressure, decreasing concentration of NaCl , and decreasing temperature. The mixture of $(\text{H}_2\text{S} + \text{CO}_2)$ may be more soluble than H_2S and even more soluble than CO_2 under cer-

tain conditions. The dissolution of H_2S will decrease the solution density in contrast to the dissolution of CO_2 . The dissolution of $(\text{H}_2\text{S} + \text{CO}_2)$ may decrease or increase the solution density, depending on the mole fraction of H_2S .

While the EOS may find many geological applications, one immediate application is to geological carbon sequestration. Co-injection of CO_2 and H_2S may substantially reduce the capture costs of carbon sequestration. However, the increased costs and risks for transportation and storage can be only evaluated when the phase equilibrium and thermodynamic properties for H_2S – CO_2 – H_2O – NaCl are understood.

ACKNOWLEDGEMENT

XJ thanks the Swedish Research Council for financial support and Professor Gerd Maurer at the University of Kaiserslautern in Germany for discussion. CZ acknowledges the support of the US Department of Energy Grant DE-FE0004381, the support from the Norwegian Center of Excellence Subsurface CO_2 storage – Critical Elements and Superior Strategy (SUCCESS), and a Fulbright scholarship to Norway. Assistance from Zhang Qian for literature search and Laura Brant for editing is acknowledged.

APPENDIX A: EOS SAFT2

The dimensionless residual Helmholtz free energy in SAFT2 is defined as follows

$$\tilde{a}^{\text{res}} = \tilde{a}^{\text{hs}} + \tilde{a}^{\text{disp}} + \tilde{a}^{\text{chain}} + \tilde{a}^{\text{assoc}} + \tilde{a}^{\text{ion}} \quad (\text{A1})$$

where the superscripts on the right side refer to terms accounting for the hard-sphere, dispersion, chain, association, and ionic interactions, respectively. In the expression of each term below, for the systems of interest, the word ‘component’ refers to CO_2 , H_2S , H_2O , Na^+ , and Cl^- .

The terms for hard-sphere, dispersion and chain have been summarized in the recent published article for heterosegmented molecules (Ji and Adidharma, 2012). In this work, all the components were modeled as homosegmented molecules, and the terms for hard-sphere and dispersion terms are exactly the same as those in heterosegmented SAFT. While for the chain term, the bond fraction is one for all types of bond in homosegmented SAFT. For completeness, the corresponding content on the hard-sphere, dispersion, and chain terms in our previous work (Ji and Adidharma, 2012) was repeatedly described in the following text. The association and ionic terms are also re-summarized in this work.

A.1. Hard-sphere term \tilde{a}^{hs} (Ji and Adidharma, 2012)

The hard-sphere contribution \tilde{a}^{hs} in heterosegmented SAFT is given by

$$\tilde{a}^{\text{hs}} = \frac{6}{\pi N_A v \rho_m} \left[\frac{(\zeta_2)^3 + 3\zeta_1\zeta_2\zeta_3 - 3\zeta_1\zeta_2(\zeta_3)^2}{\zeta_3(1 - \zeta_3)^2} - \left(\zeta_0 - \frac{(\zeta_2)^3}{(\zeta_3)^2} \right) \ln(1 - \zeta_3) \right] \quad (\text{A2})$$

Table A1

The universal coefficients c_{ij} in Eq. (A13) (Tan et al., 2006).

i/j	1	2	3	4	5	6
1	−0.010 348 412 43	5.012 940 585	−46.069 085 85	271.226 970 3	−645.515 037 9	605.117 779 9
2	0.034 371 512 70	−45.703 391 47	391.844 391 2	−2296.265 301	5430.859 895	−5087.008 598
3	0.046 688 853 54	161.837 063 5	−1267.473 745	7368.693 459	−17,288.510 83	16,217.305 15
4	−0.286 193 974 80	−276.070 506 3	1903.020 452	−10,912.042 77	25,296.495 02	−23,885.063 01
5	0.679 398 501 40	224.732 718 6	−1256.163 441	7025.297 671	−15,911.317 81	15,336.690 52
6	−1.380 935 033	−69.715 059 55	242.462 559 3	−1282.236 283	2690.356 186	−2828.288 422

where N_{Av} is the Avogadro number, ρ_m is the molar density, and

$$\zeta_k = \frac{\pi}{6} N_{Av} \rho_m \sum_i X_i m_i \sum_\alpha x_\alpha (\sigma_\alpha)^k \quad (k = 0, 1, 2, 3) \quad (\text{A3})$$

where X_i is the mol fraction of component i , m_i is the number of segments of component i , σ_α is the diameter of segment α , and x_α is the segment fraction defined as

$$x_\alpha = \frac{\text{Number of moles of segments } \alpha}{\text{Number of moles of all segments}} \quad (\text{A4})$$

A.2. Dispersion term \tilde{a}^{disp} (Ji and Adidharma, 2012)

The dispersion term is calculated from

$$\tilde{a}^{\text{disp}} = \sum_i X_i m_i \left[\frac{1}{k_B T} a_1^{\text{disp}} + \frac{1}{(k_B T)^2} a_2^{\text{disp}} + \tilde{a}' \right] \quad (\text{A5})$$

where k_B is the Boltzmann constant, T is the temperature in Kelvin, and

$$a_1^{\text{disp}} = \sum_\alpha \sum_\beta x_\alpha x_\beta a_{1,\alpha\beta}^{\text{disp}} \quad (\text{A6})$$

where α and β are the segment types, and $a_{1,\alpha\beta}^{\text{disp}}$ is the first-order binary term for α – β segment interaction given by

$$a_{1,\alpha\beta}^{\text{disp}} = -4 \left(\frac{\pi}{6} \sigma_{\alpha\beta}^3 N_{Av} \rho_m \right) u_{\alpha\beta} (\lambda_{\alpha\beta}^3 - 1) g_{\alpha\beta}^{\text{hs}}(\sigma_{\alpha\beta}, \zeta_{3,\text{eff}}) \quad (\text{A7})$$

In Eq. (A7), $\sigma_{\alpha\beta}$ is the distance between centers of segment α and β at contact, $u_{\alpha\beta}$ is the well depth of square-well potential for the α – β interaction, and $\lambda_{\alpha\beta}$ is the reduced range of the potential well for the α – β interaction. The combining rules used for $\sigma_{\alpha\beta}$ and $u_{\alpha\beta}$ are,

$$\sigma_{\alpha\beta} = \frac{1}{2} (\sigma_\alpha + \sigma_\beta) \quad (\text{A8})$$

$$u_{\alpha\beta} = u_{\beta\alpha} = \sqrt{u_\alpha u_\beta} (1 - k_{\alpha\beta}) \quad (\text{A9})$$

where u_α is the segment energy of segment α , and $k_{\alpha\beta}$ is the binary interaction parameter which can be temperature-dependent or temperature-independent.

A simple arithmetic-mean combining rule is used for $\lambda_{\alpha\beta}$, analogous to that for the segment diameters:

$$\lambda_{\alpha\beta} = \frac{1}{2} (\lambda_\alpha + \lambda_\beta) \quad (\text{A10})$$

where λ_α is the reduced range of the potential well of segment α .

The radial distribution function for a mixture of hard spheres in Eq. (A7) is calculated using Carnahan–

Starling's equation but evaluated at the effective reduced variable ζ_{keff} ,

$$g_{\alpha\beta}^{\text{hs}}(\sigma_{\alpha\beta}, \zeta_{3,\text{eff}}) = \frac{1}{1 - \zeta_{3,\text{eff}}} + \frac{3\sigma_\alpha\sigma_\beta}{\sigma_\alpha + \sigma_\beta} \frac{\zeta_{2,\text{eff}}}{(1 - \zeta_{3,\text{eff}})^2} + 2 \left(\frac{\sigma_\alpha\sigma_\beta}{\sigma_\alpha + \sigma_\beta} \right)^2 \frac{(\zeta_{2,\text{eff}})^2}{(1 - \zeta_{3,\text{eff}})^3} \quad (\text{A11})$$

In the range of $1.0 < \lambda_{\alpha\beta} \leq 2.5$, the effective reduced variable $\zeta_{3,\text{eff}}$ is approximated from

$$\zeta_{3,\text{eff}}(\lambda_{\alpha\beta}, \zeta_3) = \zeta_3 [1 + \delta(\lambda_{\alpha\beta}, \zeta_3)] \quad (\text{A12})$$

where

$$\delta(\lambda_{\alpha\beta}, \zeta_3) = \lambda_{\alpha\beta}^{5.397} (\lambda_{\alpha\beta} - 1) (1 - 0.59\zeta_3) \sum_{i=1}^6 \sum_{j=1}^6 c_{ij} \frac{\zeta_3^{i-1}}{\lambda_{\alpha\beta}^{j-1}} \quad (\text{A13})$$

and c_{ij} 's are universal constants listed in Table A1.

In Eq. (A12), the effective reduced variable $\zeta_{2,\text{eff}}$ is calculated from

$$\zeta_{2,\text{eff}} = \frac{\zeta_2}{\zeta_3} \zeta_{3,\text{eff}} \quad (\text{A14})$$

The term a_2^{disp} in Eq. (A5) has the same form as the term a_1^{disp} ,

$$a_2^{\text{disp}} = \sum_\alpha \sum_\beta x_\alpha x_\beta a_{2,\alpha\beta}^{\text{disp}} \quad (\text{A15})$$

where $a_{2,\alpha\beta}^{\text{disp}}$ is related to $a_{1,\alpha\beta}^{\text{disp}}$ as follows:

$$a_{2,\alpha\beta}^{\text{disp}} = \frac{1}{2} u_{\alpha\beta} \rho_m \frac{\partial a_{1,\alpha\beta}^{\text{disp}}}{\partial \rho_m} \left(\frac{\zeta_0(1 - \zeta_3)^4}{\zeta_0(1 - \zeta_3)^2 + 6\zeta_1\zeta_2(1 - \zeta_3) + 9\zeta_2^3} \right) \quad (\text{A16})$$

The term \tilde{a}' in Eq. (A5) is calculated from

$$\tilde{a}' = \sum_{m=2}^5 \sum_{n=1}^2 D_{mn} \left(\frac{u}{k_B T} \right)^m \left(\frac{\zeta_3}{\tau} \right)^n \quad (\text{A17})$$

where D_{mn} 's are universal constants listed in Table A2, τ is the close-packed reduced density ($= 2^{1/2} \pi/6$), and $u/k_B T$ is evaluated in the spirit of the van der Waals one fluid theory

Table A2

The universal coefficients D_{mn} in Eq. (A17) (Tan et al., 2006).

n/m	2	3	4	5
1	−2.420747	−4.151326	2.501130	−0.462574
2	9.955897	−1.520369	0	0

$$\frac{u}{kT} = \frac{\sum_{\alpha} \sum_{\beta} x_{\alpha} x_{\beta} \left(\frac{u_{\alpha\beta}}{k_B T} \right) v_{\alpha\beta}}{\sum_{\alpha} \sum_{\beta} x_{\alpha} x_{\beta} v_{\alpha\beta}} \quad (\text{A18})$$

where

$$v_{\alpha\beta} = \left[\frac{(v_{\alpha})^{1/3} + (v_{\beta})^{1/3}}{2} \right]^3 \quad (\text{A19})$$

The molar volume of segment α (v_{α}) is related to the segment diameter as follows:

$$v_{\alpha} = \frac{\pi}{6\tau} \sigma_{\alpha}^3 N_{Av} \quad (\text{A20})$$

A.3. Chain term \tilde{a}^{chain} (Ji and Adidharma, 2012)

The chain term is calculated by

$$\tilde{a}^{\text{chain}} = - \sum_i X_i (m_i - 1) [\ln \bar{g}_i^{\text{SW}}(\sigma_{\alpha\beta}) - \ln \bar{g}_{0,i}^{\text{SW}}(\sigma_{\alpha\beta})] \quad (\text{A21})$$

and

$$\ln \bar{g}_i^{\text{SW}}(\sigma_{\alpha\beta}) = \sum_{\beta \geq \alpha} B_{\alpha\beta,i} \ln g_{\alpha\beta}^{\text{SW}}(\sigma_{\alpha\beta}) \quad (\text{A22})$$

where $g_{\alpha\beta}^{\text{SW}}(\sigma_{\alpha\beta})$ is the square-well radial distribution function calculated at contact, and $\bar{g}_{0,i}^{\text{SW}}$ is \bar{g}_i^{SW} evaluated at zero density. The pair radial distribution function for a mixture of square-well segments is determined as follows

$$g_{\alpha\beta}^{\text{SW}}(\sigma_{\alpha\beta}) = g_{\alpha\beta}^{\text{hs}}(\sigma_{\alpha\beta}) + \beta u_{\alpha\beta} g_{1,\alpha\beta}(\sigma_{\alpha\beta}) \quad (\text{A23})$$

where $g_{\alpha\beta}^{\text{hs}}(\sigma_{\alpha\beta})$ is the pair radial distribution function for a mixture of hard sphere given by

$$g_{\alpha\beta}^{\text{hs}}(\sigma_{\alpha\beta}) = \frac{1}{1 - \zeta_3} + \frac{3\sigma_{\alpha}\sigma_{\beta}}{\sigma_{\alpha} + \sigma_{\beta}} \frac{\zeta_2}{(1 - \zeta_3)^2} + 2 \left[\frac{\sigma_{\alpha}\sigma_{\beta}}{\sigma_{\alpha} + \sigma_{\beta}} \right]^2 \frac{(\zeta_2)^2}{(1 - \zeta_3)^3} \quad (\text{A24})$$

and $g_{1,\alpha\beta}(\sigma_{\alpha\beta})$ is the perturbation term,

$$g_{1,\alpha\beta}(\sigma_{\alpha\beta}) = \frac{1}{4u_{\alpha\beta}} \left[\frac{1}{\frac{\pi}{6} \sigma_{\alpha\beta}^3 N_{Av} \sum_i X_i m_i} \frac{\partial a_{1,\alpha\beta}}{\partial \rho} - \frac{\lambda_{\alpha\beta}}{3(\frac{\pi}{6} \sigma_{\alpha\beta}^3 N_{Av} \rho \sum_i X_i m_i)} \frac{\partial a_{1,\alpha\beta}^{\text{disp}}}{\partial \lambda_{\alpha\beta}} \right] \quad (\text{A25})$$

In Eq. (A22), $B_{\alpha\beta,i}$ is the bond fraction of type $\alpha\beta$ in molecule of component i and it is equal to one since each component studied in this work is a homosegmented molecule.

A.4. Association term \tilde{a}^{assoc}

The association term is calculated by Adidharma and Radosz (2001)

$$\tilde{a}^{\text{assoc}} = \sum_i X_i \left[\sum_{A_i \in \Gamma_i} \left(\ln X^{A_i} - \frac{X^{A_i}}{2} \right) + \frac{n(\Gamma_i)}{2} \right] \quad (\text{A26})$$

where $n(i)$ is the number of association sites on molecule i and X^{A_i} is the mole fraction of molecules i not bonded at site A_i given by

$$X^{A_i} = \frac{1}{1 + \rho_n \sum_j \left[X_j \sum_{B_j \in \Gamma_j} (X^{B_j} \Delta^{A_i B_j}) \right]} \quad (\text{A27})$$

where $\Delta^{A_i B_j}$ is the association strength between site A_i at molecule i and site B_j at molecule j given by

$$\Delta^{A_i B_j} = F^{A_i B_j} e^{\beta \Delta(\rho) u_{ij}} g^{\text{hs}}(\sigma_{ij}) (\sigma_{ij}^3 \kappa^{A_i B_j}) \quad (\text{A28})$$

where

$$F^{A_i B_j} = \exp(\varepsilon^{A_i B_j} / k_B T) - 1 \quad (\text{A29})$$

and

$$\alpha(\rho) = 1 + 0.1044\rho^* - 2.8469(\rho^*)^2 + 2.3787(\rho^*)^3 \quad (\text{A30})$$

where ρ^* is the reduced density related to the segment density ρ_s by

$$\rho^* = \frac{6}{\pi} \sum_{\alpha} \sum_{\beta} x_{\alpha} x_{\beta} \sigma_{\alpha\beta}^3 \quad (\text{A31})$$

The Lorentz and Berthelot combining rules are used for the size and energy parameters, i.e.

$$\sigma_i = \left(\frac{\sqrt{2}}{N_{Av}} v^{oo} \right)^{\frac{1}{3}} \quad (\text{A32})$$

$$\sigma_{ij}^3 \kappa^{A_i B_j} = \left[\frac{(\sigma_i^3 \kappa^{A_i B_i})^{1/3} + (\sigma_j^3 \kappa^{A_j B_j})^{1/3}}{2} \right]^3 \quad (\text{A33})$$

$$\varepsilon^{A_i B_j} = \sqrt{\varepsilon^{A_i B_i} \varepsilon^{A_j B_j}} \quad (\text{A34})$$

A.5. Ionic term \tilde{a}^{ion}

Restricted primitive model is used in SAFT2 to account for long-range Coulomb interactions (Tan et al., 2005)

$$\tilde{a}^{\text{ion}} = - \frac{3X^2 + 6X + 2 - 2(1 + 2X)^{3/2}}{12\pi\rho_m N_{Av} d^3} \quad (\text{A35})$$

where d is the effective (hydrated) diameter defined by

$$d = \sum_i x'_i d_i \quad (\text{A36})$$

where x'_i is the mole fraction of ion i on a solvent-free basis and the summation is over all ions. In Eq. (A35), X is the dimensionless quantity defined by

$$X = \kappa d \quad (\text{A37})$$

where κ is the Debye inverse screening length given by

$$\kappa^2 = \frac{4\pi}{\varepsilon_w k_B T} \sum_j \rho_{n,j} q_j^2 = \frac{4\pi e^2}{\varepsilon_w k_B T} \sum_j \rho_{n,j} z_j^2 \quad (\text{A38})$$

where ε_w is the dielectric constant of water, $\rho_{n,j}$ is the number density of ion j , q_j is the charge of ion j ($=z_j e$), z_j is the valence of the ion j , e is the charge of an electron, and the summation is over all ions in the mixture.

APPENDIX B. PARAMETERS IN THE COMPONENT SUBSYSTEMS

B.1. Pure components

For the system of interest in this work, the components of H₂S, H₂O and CO₂ have been investigated with SAFT2, in which H₂S was modeled as a molecule with four association sites, i.e. two sites of type S and two sites of type H. H₂O was also modeled as a molecule with four association sites, i.e. two sites of type O and two sites of type H. CO₂ was modeled as a molecule with three association sites, i.e. two sites of type O and one site of type C. Sites of the same type do not associate with each other. Parameters were obtained from the fitting of the experimental data of saturation pressure and saturation liquid densities. The fitted parameters are summarized in Table B1.

B.2. Aqueous NaCl solutions

NaCl is a special component compared to H₂S, H₂O and CO₂. It was dissociated into cation and anion in water or in the aqueous solutions of interest in this work. There are no available experimental data for pure NaCl.

In our previous work (Ji and Adidharma, 2007), the properties of a group of ions (Li⁺, Na⁺, K⁺, Ca²⁺, Mg²⁺, Cl[−], Br[−], I[−], NO₃[−], HCO₃[−], SO₄^{2−}, CO₃^{2−}) in aqueous solution were investigated with SAFT2. Each ion was modeled as charged, but non-associating, spherical segments. To account for the effect of pressure on the properties of electrolyte solutions, a short-range interaction between cation and anion was allowed, but we neglected the cation–cation and anion–anion short-range interactions, i.e., $k_{\alpha\beta} = 1$. We considered full short-range interaction between ion and water, i.e., $k_{\alpha\beta} = 0$. $k_{\alpha\beta}$ for cation–anion short-range interaction is expected to be in the range of zero to unity. For practical purposes, we set $k_{\alpha\beta} = 0.5$ for this cation–an-

ion short-range interaction, in order to reduce the number of parameters. Moreover, parameters of, u , λ and d were temperature-dependent with following equations:

$$v = v_{25}[1 + b_1(T - 298.15) + b_2(T - 298.15)^2] \quad (\text{B1})$$

$$u = u_{25}[1 + b_3(T - 298.15) + b_4(T - 298.15)^2] \quad (\text{B2})$$

$$\lambda = \lambda_{25}[1 + b_5(T - 298.15) + b_6(T - 298.15)^2] \quad (\text{B3})$$

$$d = d_{25}[1 + b_7(T - 298.15) + b_8(T - 298.15)^2] \quad (\text{B4})$$

where b_1 to b_8 are the ion-specific coefficients.

One set of parameters for this group of ions at 298.15 K was fitted to a group of experimental data and liquid density. The coefficients for temperature-dependent parameters were fitted to the experimental activity coefficients and liquid densities at temperatures up to 473.15 K and low pressures. The parameters for Na⁺ and Cl[−] are listed in Tables B2 and B3, where $\lambda_{25,i-w}$ is the arithmetic mean of the reduced well range for water–ion interactions ($\lambda_{25,i-w} = 0.5(\lambda_{25,w} + \lambda_{25,i})$, where w refers to water and i refers to cation or anion).

B.3. H₂S(1)–H₂O(3)

In our previous work (Ji and Zhu, 2010), the phase equilibrium for H₂S(1)–H₂O(3) was investigated, in which cross association between the site H in H₂S and the site O in H₂O was allowed and two temperature-dependent parameters were used to describe this cross association. Meanwhile, a temperature-dependent binary interaction parameter was used to adjust the cross dispersive energy for this binary system with the equation:

$$\frac{\varepsilon_{13}^{\text{HO}}}{k} = C_7 + C_8 T \quad (\text{B5})$$

$$\kappa_{13}^{\text{HO}} = C_9 + C_{10} T \quad (\text{B6})$$

$$k_{13} = C_{11} + C_{12} T \quad (\text{B7})$$

Table B1
Parameters for CO₂, H₂S and H₂O.

	m	v^{00} (cc/mol)	u^0/k (K)	λ	ε/k (K)	κ
CO ₂ (Ji and Adidharma, 2010)	1.3513	11.137	219.992	1.4220	217.7834	0.18817
H ₂ S (Ji and Zhu, 2010)	1.2882	11.7602	254.318	1.5240	135.62	0.004382
H ₂ O (Tan et al., 2006)	1.0	9.8307	311.959	1.5369	1481.41	0.04682

Table B2
Parameters for Na⁺ and Cl[−] at 298.15 K (25 °C).

i	v_{25} (cc)	(u_{25}/k) (K)	$\lambda_{25,i-w}$	d_{25} (Å)	i	v_{25} (cc)	(u_{25}/k) (K)	$\lambda_{25,i-w}$	d_{25} (Å)
Na ⁺	1.6961	3321.67	1.8860	4.6806	Cl [−]	7.6771	1228.19	1.0924	5.6428

Table B3
Coefficients in Eqs. (B1)–(B4).

	$10^3 b_1$ (K ^{−1})	$10^5 b_2$ (K ^{−2})	$10^3 b_3$ (K ^{−1})	$10^5 b_4$ (K ^{−2})	$10^4 b_5$ (K ^{−1})	$10^6 b_6$ (K ^{−2})	$10^4 b_7$ (K ^{−1})	$10^6 b_8$ (K ^{−2})
Na ⁺	−3.8224	−0.0022	−4.8026	2.5607	7.7334	−3.0528	0.6083	−5.0683
Cl [−]	1.5282	0.1448	−4.7972	2.1132	−0.9565	9.7282	0.0827	−5.0773

Table B4

Cs in Eqs. (B7)–(B10), (and) (B13).

Parameter	Value	Parameter	Value	Parameter	Value
C_7	1.5154×10^2	C_{14} (T)	-9.0662×10^6	C_{21}	9.2661×10^{-1}
C_8 (T ⁻¹)	2.7904×10^0	C_{15} (T ²)	3.4164×10^9	C_{22} (T ⁻¹)	-9.3469×10^{-3}
C_9	-1.8143×10^{-3}	C_{16} (T ³)	-4.3221×10^{11}	C_{23} (T ⁻²)	2.7383×10^{-5}
C_{10} (T ⁻¹)	9.6423×10^{-5}	C_{17}	1.5329×10^0	C_{24} (T ⁻³)	-2.3398×10^{-8}
C_{11}	-1.9109×10^{-1}	C_{18} (T ⁻¹)	-1.2150×10^{-2}	C_{25}	-8.0059×10^{-2}
C_{12} (T ⁻¹)	8.1684×10^{-4}	C_{19} (T ⁻²)	3.1406×10^{-5}	C_{26} (T ⁻¹)	1.4236×10^{-3}
C_{13}	9.1029×10^3	C_{20} (T ⁻³)	-2.5884×10^{-8}		

Cross parameters were fitted to mole fractions both in H₂S-rich/vapor phases and H₂O-rich phases measured experimentally. The fitted results are listed in Table B4. The model is found to represent well the phase equilibria of the H₂S–H₂O system from 273 to 630 K and at pressures up to 200 bars.

B.4. CO₂(2)–H₂O(3)–NaCl(4)

Similar to our previous work (Ji et al., 2005a), SAFT2 was used to represent the properties and phase equilibrium of the CO₂–H₂O system, in which one type of cross association was assigned, i.e. between the site of type O in CO₂ and the site of type H in H₂O. The cross association is temperature-dependent with the following equations:

$$\frac{\epsilon_{23}^{\text{OH}}}{k} = C_{13} + C_{14}T^{-1} + C_{15}T^{-2} + C_{16}T^{-3} \quad (\text{B8})$$

$$k_{23}^{\text{OH}} = C_{17} + C_{18}T + C_{19}T^2 + C_{20}T^3 \quad (\text{B9})$$

A temperature-dependent binary interaction parameter k_{23} was used to adjust the cross dispersive energy for this binary system

$$k_{23} = C_{21} + C_{22}T + C_{23}T^2 + C_{24}T^3 \quad (\text{B10})$$

For CO₂(2)–H₂O(3)–NaCl(4), a temperature-dependent binary interaction parameter, k_{24} , the same for both CO₂–Na⁺ and CO₂–Cl[−] pairs, was used to adjust the short-range interactions

$$u_{24+} = (u_{24+})^{1/2}(1 - k_{24}) \quad (\text{B11})$$

$$u_{24-} = (u_{24-})^{1/2}(1 - k_{24}) \quad (\text{B12})$$

$$k_{24} = C_{25} + (T - 273.15) \cdot C_{26} \quad (\text{B13})$$

The temperature-dependent cross parameters were directly fitted to the same experimental data as in our previous work (Ji et al., 2005a). The fitted results are listed in Table B4.

APPENDIX C. SUPPLEMENTARY DATA

Supplementary data associated with this article can be found, in the online version, at <http://dx.doi.org/10.1016/j.gca.2012.05.023>.

REFERENCES

- Adidharma H. and Radosz M. (2001) Saft1 for associating fluids: alkanols. *J. Phys. Chem. B* **105**, 9822–9827.
- Bachu S. and Bennion D. B. (2009) Chromatographic partitioning of impurities contained in a co2 stream injected into a deep

- saline aquifer: Part 1. Effects of gas composition and in situ conditions. *Int. J. Greenhouse Gas Control* **3**(4), 458–467.
- Bachu S. and Carroll J.J. (2005) In-situ phase and thermodynamic properties of resident brine and acid gases (CO₂ and H₂S) injected in geological formations in western Canada: demonstration of CO₂ geological storage, Carbon Dioxide Capture for Storage. In *Deep Geologic Formations – Results from the CO₂ Capture Project, v. 2: Geologic Storage of Carbon Dioxide with Monitoring and Verification* (ed. S. M. Benson). Elsevier, London. pp. 867–876.
- Bachu S. and Gunter W. D. (2004) Acid gas injection in the Alberta basin, Canada: a CO₂ storage experience. *Geological Storage of Carbon Dioxide. Geol. Soc. London Spec. Publ.* **233**, 225–234.
- Bachu S. and Watson T. L. (2009) Review of failures for wells used for CO₂ and acid gas injection in Alberta, Canada. *Energy Procedia* **1**(1), 3531–3537.
- Bachu S., Buschkuehle M., Haug K. and Michael K. (2008a) Subsurface characterization of the Edmonton-area acid-gas injection operations. *Energy Resources Conservation Board, ERCB/AGS Special Report 092*, 134p.
- Bachu S., Buschkuehle M., Haug K. and Michael K. (2008b) Subsurface characterization of the Pembina-Wabamun acid-gas injection operations. *Energy Resources Conservation Board, ERCB/AGS Special Report 093*, 60p.
- Barrett T. J., Anderson G. M. and Lugowski J. (1988) The solubility of hydrogen sulphide in 0–5 m NaCl solutions at 25°–95 °C and one atmosphere. *Geochim. Cosmochim. Acta* **52**(4), 807–811.
- Bierlein J. and Kay W. B. (1953) Phase-equilibrium properties of system carbon dioxide-hydrogen sulfide. *Ind. Eng. Chem.* **45**(3), 618–624.
- Buschkuehle B. E. and Michael K. (2006) Subsurface characterization of acid-gas injection operations in northeastern British Columbia. *Alberta Energy and Utilities Board, EUB/AGS Earth Sciences Report 2006–05*, 201 p.
- dos Ramos M. C. and McCabe C. (2010) Modeling the phase behavior, excess enthalpies and henry's constants of the H₂O + H₂S binary mixture using the saft-vr plus d approach. *Fluid Phase Equilib.* **290**(1–2), 137–147.
- Drummond S. E. (1981) Boiling and mixing of hydrothermal fluids: chemical effects on mineral precipitation. Ph. D. dissertation, Pennsylvania state university.
- Duan Z. H. and Li D. D. (2008) Coupled phase and aqueous species equilibrium of the H₂O–CO₂–NaCl–CaCO₃ system from 0 to 250 degrees C, 1 to 1000 bar with NaCl concentrations up to saturation of halite. *Geochim. Cosmochim. Acta* **72**(20), 5128–5145.
- Duan Z. H., Moller N. and Weare J. H. (1996) Prediction of the solubility of H₂S in NaCl aqueous solution: an equation of state approach. *Chem. Geol.* **130**(1–2), 15–20.
- Duan Z. H., Sun R., Liu R. and Zhu C. (2007) Accurate thermodynamic model for the calculation of h2s solubility in pure water and brines. *Energy Fuels* **21**(4), 2056–2065.

- Dubessy J., Tarantola A. and Sterpenich J. (2005) Modelling of liquid–vapour equilibria in the H_2O – CO_2 – NaCl and H_2O – H_2S – NaCl systems to 270 degrees C. *Oil Gas Sci. Technol. Rev. IFP* **60**(2), 339–355.
- Gunter W. D., Perkins E. H. and Hutcheon I. (2000) Aquifer disposal of acid gases: modeling of water–rock reactions for trapping of acid wastes. *Appl. Geochem.* **15**(8), 1085–1095.
- IPCC (2005) IPCC Special Report on carbon dioxide capture and storage. Prepared by Working Group III of the Intergovernmental Panel on Climate Change. In: B. Metz, O. Davidson, H. C. de Coninck, M. Loos and L. A. Meyer (eds.). Cambridge University Press.
- Ji X. Y. and Adidharma H. (2006) Ion-based saft2 to represent aqueous single- and multiple-salt solutions at 298.15 k. *Ind. Eng. Chem. Res.* **45**(22), 7719–7728.
- Ji X. Y. and Adidharma H. (2007) Ion-based statistical associating fluid theory (SAFT2) to represent aqueous single-salt solutions at temperatures and pressures up to 473.15 k and 1000 bar. *Ind. Eng. Chem. Res.* **46**(13), 4667–4677.
- Ji X. Y. and Adidharma H. (2008) Ion-based SAFT2 to represent aqueous multiple-salt solutions at ambient and elevated temperatures and pressures. *Chem. Eng. Sci.* **63**(1), 131–140.
- Ji X. Y. and Adidharma H. (2009) Thermodynamic modeling of ionic liquid density with heterosegmented statistical associating fluid theory. *Chem. Eng. Sci.* **64**(9), 1985–1992.
- Ji X. Y. and Adidharma H. (2010) Thermodynamic modeling of CO_2 solubility in ionic liquid with heterosegmented statistical associating fluid theory. *Fluid Phase Equilib.* **293**(2), 141–150.
- Ji X. Y. and Adidharma H. (2012) Prediction of molar volume and partial molar volume for CO_2 /ionic liquid systems with heterosegmented statistical associating fluid theory. *Fluid Phase Equilib.* **315**, 53–63.
- Ji X. Y. and Zhu C. (2010) Modelling of phase equilibria in the H_2S – H_2O system with statistical associating fluid theory. *Energy Fuels* **24**, 6208–6213.
- Ji X. Y., Tan S. P., Adidharma H. and Radosz M. (2005a) Saft1-rpm approximation extended to phase equilibria and densities of CO_2 – H_2O and CO_2 – H_2O – NaCl systems. *Ind. Eng. Chem. Res.* **44**(22), 8419–8427.
- Ji X. Y., Tan S. P., Adidharma H. and Radosz M. (2005b) Statistical associating fluid theory coupled with restricted primitive model to represent aqueous strong electrolytes: multiple-salt solutions. *Ind. Eng. Chem. Res.* **44**(19), 7584–7590.
- Ji X. Y., Tan S. P., Adidharma H. and Radosz M. (2006) Statistical associating fluid theory coupled with restrictive primitive model extended to bivalent ions. Saft2: 2. Brine/seawater properties predicted. *J. Phys. Chem. B* **110**(33), 16700–16706.
- Ji Y. H., Ji X. Y., Feng X., Liu C., Lu L. H. and Lu X. H. (2007) Progress in the study on the phase equilibria of the CO_2 – H_2O and CO_2 – H_2O – NaCl systems. *Chin. J. Chem. Eng.* **15**(3), 439–448.
- Knauss K. G., Johnson J. W. and Steefel C. I. (2005) Evaluation of the impact of CO_2 , co-contaminant gas, aqueous fluid and reservoir rock interactions on the geologic sequestration of CO_2 . *Chem. Geol.* **217**(3–4), 339–350.
- Li Z. D. and Firoozabadi A. (2009) Cubic-plus-association equation of state for water-containing mixtures: is “cross association” necessary? *AIChE J.* **55**(7), 1803–1813.
- Micheal K. and Buschkuehle M. (2008a) Subsurface characterization of acid-gas injection operations in the Peace River Arch Area. *Energy Resources Conservation Board, ERCB/AGS Special Report 090*, 186p.
- Micheal K. and Buschkuehle M. (2008b) Subsurface characterization of acid-gas injection operations in the Provost Area. *Energy Resources Conservation Board, ERCB/AGS Special Report 091*, 143p.
- Palandri J. L. and Kharaka Y. K. (2005) Ferric iron-bearing sediments as a mineral trap for CO_2 sequestration: iron reduction using sulfur bearing waste gas. *Chem. Geol.* **217**(3–4), 351–364.
- Pappa G. D., Perakis C., Tsimpanogiannis I. N. and Voutsas E. C. (2009) Thermodynamic modeling of the vapor–liquid equilibrium of the CO_2 / H_2O mixture. *Fluid Phase Equilib.* **284**(1), 56–63.
- Perfetti E., Thiery R. and Dubessy J. (2008a) Equation of state taking into account dipolar interactions and association by hydrogen bonding. I: application to pure water and hydrogen sulfide. *Chem. Geol.* **251**(1–4), 58–66.
- Perfetti E., Thiery R. and Dubessy J. (2008b) Equation of state taking into account dipolar interactions and association by hydrogen bonding: II – modelling liquid–vapour equilibria in the H_2O – H_2S , H_2O – CH_4 and H_2O – CO_2 systems. *Chem. Geol.* **251**(1–4), 50–57.
- Sobocinski D. P. and Kurata F. (1959) Heterogeneous phase equilibria of yjr hydrogen sulfide–carbon dioxide system. *AIChE J.* **5**(4), 545–551.
- Spycher N. and Pruess K. (2010) A phase-partitioning model for CO_2 –brine mixtures at elevated temperatures and pressures: application to CO_2 -enhanced geothermal systems. *Transp. Porous Media* **82**(1), 173–196.
- Spycher N., Pruess K. and Ennis-King J. (2003) CO_2 – H_2O mixtures in the geological sequestration of CO_2 . I. Assessment and calculation of mutual solubilities from 12 to 100 degrees C and up to 600 bar. *Geochim. Cosmochim. Acta* **67**(16), 3015–3031.
- Stouffer C. E., Kellerman S. J., Hall K. R., Holste J. C., Gammon B. E. and Marsh K. N. (2001) Densities of carbon dioxide plus hydrogen sulfide mixtures from 220 k to 450 k at pressures up to 25 mpa. *J. Chem. Eng. Data* **46**(5), 1309–1318.
- Suleimenov O. M. and Krupp R. E. (1994) Solubility of hydrogen sulfide in pure water and in NaCl solutions, from 20 to 320 degree C and at saturation pressures. *Geochim. Cosmochim. Acta* **58**(11), 2433–2444.
- Sun R. and Dubessy J. (2010) Prediction of vapor–liquid equilibrium and pvt properties of geological fluid system with saft-lj eos including multi-polar contribution. Part i: application to H_2O – CO_2 system. *Geochim. Cosmochim. Acta* **74**(7), 1982–1998.
- Tan S. P., Adidharma H. and Radosz M. (2005) Statistical associating fluid theory coupled with restricted primitive model to represent aqueous strong electrolytes. *Ind. Eng. Chem. Res.* **44**(12), 4442–4452.
- Tan S. P., Ji X. Y., Adidharma H. and Radosz M. (2006) Statistical associating fluid theory coupled with restrictive primitive model extended to bivalent ions. Saft2: 1. Single salt plus water solutions. *J. Phys. Chem. B* **110**(33), 16694–16699.
- Tang X. H. and Gross J. (2010) Modeling the phase equilibria of hydrogen sulfide and carbon dioxide in mixture with hydrocarbons and water using the pc-p-saft equation of state. *Fluid Phase Equilib.* **293**(1), 11–21.
- Xia J. Z., Kamps A. P. S., Rumpf B. and Maurer G. (2000) Solubility of hydrogen sulfide in aqueous solutions of the single salts sodium sulfate, ammonium sulfate, sodium chloride, and ammonium chloride at temperatures from 313 to 393 k and total pressures up to 10 mpa. *Ind. Eng. Chem. Res.* **39**(4), 1064–1073.
- Xiao Y., Xu T. and Pruess K. (2009) The effects of gas–fluid–rock interactions on CO_2 injection and storage: insights from

- reactive transport modeling. *Energy Procedia* **1**(1), 1783–1790.
- Xu T., Apps J. A., Pruess K. and Yamamoto H. (2007) Numerical modeling of injection and mineral trapping of CO₂ with H₂S and SO₂ in a sandstone formation. *Chem. Geol.* **242**(3–4), 319–346.
- Yang C. D. and Gu Y. G. (2006) Accelerated mass transfer of CO₂ in reservoir brine due to density-driven natural convection at high pressures and elevated temperatures. *Ind. Eng. Chem. Res.* **45**(8), 2430–2436.

Associate editor: Peter Ulmer